

UNIVERSITY OF OKLAHOMA
GRADUATE COLLEGE

NON-DESTRUCTIVE EXAMINATION OF CERAMIC MATRIX COMPOSITES FOR
QUANTITATIVE DETERMINATION OF POROSITY VIA PULSE-ECHO
THERMOGRAPHIC INSPECTION

A THESIS
SUBMITTED TO THE GRADUATE FACULTY
in partial fulfillment of the requirements for the
Degree of
MASTER OF SCIENCE

By

ROSS MOSELEY
Norman, Oklahoma
2021

NON-DESTRUCTIVE EXAMINATION OF CERAMIC MATRIX COMPOSITES FOR
QUANTITATIVE DETERMINATION OF POROSITY VIA PULSE-ECHO
THERMOGRAPHIC INSPECTION

A THESIS APPROVED FOR THE
SCHOOL OF AEROSPACE AND MECHANICAL ENGINEERING

BY THE COMMITTEE CONSISTING OF

Dr. Zahed Siddique, Chair

Dr. Feng Lai

Dr. M. Cengiz Altan

© Copyright by ROSS MOSELEY 2021
All Rights Reserved.

Dedicated to my beautiful wife Brittany, without whom I would never have made it through this journey. I love you, Älskling.

“Being an American scientist sucks sometimes. You think in random, unpredictable units based on what situation you’re in.”

-Andy Weir

Acknowledgements

This thesis has been a journey in assistance and there are many, many people who deserve recognition here. The first among them is my wonderful wife Brittany who has supported me, inspired me, and told me to get to work when I needed it throughout this entire process. I could not have finished this without her.

This work would not have been possible without the constant support of Dr. Zahed Siddique, who has mentored and guided me for over a decade now, thank you for everything over the years. There are many others at OU who deserve thanks. Thank you to Dr. M. Cengiz Altan and Dr. Feng Lai for being on my committee, even when it was months and months since we had last talked, and for the advice and guidance you gave me. Thank you to Dr's Hong Liu and Yuhua Li for helping me to gather the Computed Tomography data for this research. Thank you to Dr. Keisha Walters and the rest of the PolySEL group for your support and inspiration to keep going when I was struggling the find the motivation to put another word on the page. And thank you Bethany Burklund for helping me with calendars and when I just didn't know whom to email.

The research of this investigation would not have been completed without the kind assistance of Dr. Steven Shepard of Thermal Wave Imaging Inc., and the time of his team Tasdiq, Bharat, and Jake. The assistance of TWI made all the thermographic inspections by this investigation possible and were essential in completing this research. Thank you so much again for all that you contributed to this project.

The most important sample set for this research was provided through the wonderful support of COI Ceramics, specifically with great thanks to Jane Minnocci and Tim Easler.

A huge thank you to all of those at the Air Force who enabled me to take part in the Long Term Training program and pursue this dream; Julie Hines, Andy Noble, and Dr. Kristian Olivero

chief among them. Thank you to Dr. Eric Lindgren for pushing me down this path and pushing me to finish every time I saw him. Thank you to Dr. Craig Pryzbyla for the initial clue on CMCs and putting me in contact with the right people, Travis Whitlow and Jennifer Pierce, also of AFRL, who deserve a thank you for the use of the large plate CMCs. Thank you to Alanna Abels, Beth Huelskamp, and Rich Smith for the aircraft components you lent to me. And thank you to Shaun Harris and Tracy McGeehee for helping me collect the radiographic data.

Thank you to my parents for all the support, comments, and editing you have put into this paper. It would not be nearly what it is without you. Thank you to the Cyrs for all of your positivity when I needed it. Thank you to Blake Harms for guilting me into working and providing entertainment when I wasn't. There has been too much support to think about during this entire process and I am constantly touched by it all. I am sure I forgot many people who gave me the small encouragements and assistances that I need to get through this so thank you to all of you.

Table of Contents

Acknowledgements.....	v
Table of Contents.....	vii
List of Tables.....	x
List of Figures.....	xi
Abstract.....	xiii
Chapter 1: Introduction.....	1
1.1 Non-Destructive Testing.....	1
1.2 Composite Materials.....	2
1.3 Ceramic Matrix Composites.....	3
1.4 NDT of Composite Materials.....	4
1.5 Research Motivation.....	6
1.6 Research Objectives and Investigative Approach.....	9
1.7 Thesis Organization.....	10
Chapter 2: The Science of Non-Destructive Inspection.....	11
2.1 Non-Destructive Inspection Basics.....	11
2.2 Radiography.....	14
2.3 Computed Tomography.....	19
2.4 Flash Thermography.....	21
Chapter 3: Ceramic Matrix Composites and Samples.....	33
3.1 Ceramic Matrix Composites.....	33
3.2 S200 Ceramic Matrix Composite Material.....	34
3.3 Sample Sets.....	37

3.3.1 Set 1: Large Plates.....	38
3.3.2 Set 2: Representative Aircraft Components	38
3.3.3 Set 3: Porosity Coupon Set.....	39
Chapter 4: Testing & Data Processing Methodology	41
4.1 Testing Methods & Data Processing.....	41
4.2 The Archimedes Method.....	42
4.3 Radiography	42
4.4 Computed Tomography	46
4.5 Flash Thermography	47
Chapter 5: Results & Analysis.....	53
5.1 Archimedes Results	53
5.2 Radiographic Results	54
5.3 Computed Tomography Results	55
5.4 Flash Thermography Results	57
5.5 Analysis.....	60
Chapter 6: Conclusions & Future Work	69
6.1 Conclusions.....	69
6.1.1 Archimedes Testing	69
6.1.2 Film Radiography Testing.....	70
6.1.3 Computed Tomography Testing.....	71
6.1.4 Flash Thermography Testing	72
6.1.5 Summary	73
6.2 Future Work	74
References.....	76
Appendix A: MATLAB Code	82

A.A.1: AreaAnalysis.m.....	82
A.A.2: RawTiffConvert.m	83
A.A.3: ThresholdImage.m	83

List of Tables

Table 1: Defects detected by NDT (adapted from ASTM E2533-09) [10]	5
Table 2: NDT methods used by sample set.....	41
Table 3: Corresponding scales of radiographic film optical transmittance [17].....	45
Table 4: Archimedes porosities of Set 1	53
Table 5: Archimedes porosities of Set 3	54
Table 6: Interrogation grid data taken from sample 4 of Set 3	55
Table 7: Average film density for all samples of Set 3	55
Table 8: CT porosity data for samples 4 & 7 from Set 3	56
Table 9: Thermographic t^* data averages for Set 3	59
Table 10: Archimedes porosity, thermographic t^* , and radiographic film density results for Set 3	60
Table 11: Archimedes and CT porosity, thermographic t^* , and radiographic film density for samples 4 & 7 of Set 3	60
Table 12: Set 3 Archimedes porosity, thickness, thermographic t^* , & calculated α	65
Table 13: Set 1 Archimedes porosity, thickness, thermographic t^* , & calculated α	66
Table 14: Set 1 Archimedes porosity & thermographically calculated porosity	67
Table 15: Set 2 Thermographic t^* , calculated thermal diffusivity and porosity	68

List of Figures

Figure 1: Aloha Airlines Flight 243 [20]	7
Figure 2: Failed fan disk from UA232 [22]	8
Figure 3: Fractured fan blade #11 from UA1175 [23].....	8
Figure 4: The first radiograph, hand of Röntgen’s wife, Anna.....	15
Figure 5: Radiographic image of a weld with inclusions (bright spots) [55]	19
Figure 6: Visual representation of CT data [31]	20
Figure 7: Heat conduction through an infinite slab, log surface temp vs log time [45]	29
Figure 8: Heat conduction through material with insulated bottom surface, log surface temp vs log time [45].....	29
Figure 9: Log surface temp vs log time graphs for inclusions of lower and higher conductivity [45].....	30
Figure 10: Defects in CMCs as thermographically imaged, metal inclusion and disbond.....	31
Figure 11: Effects on density of increasing PIP cycles for CMCs of various matrix materials [51]	36
Figure 12: Samples 1450 and 1461 of Set 1	38
Figure 13: Samples from Set 3 arranged by decreasing porosity	39
Figure 15: Standard USAF radiographic tube head [56]	44
Figure 14: Diagram of radiographic exposure [17]	44
Figure 16: X-Rite 301 Densitometer [57]	45
Figure 17: Perkin Elmer quantum FX microCT [58].....	46
Figure 18: Commercial EchoTherm thermographic inspection system [59].....	48
Figure 19: Stills from thermographic investigation of Set 3 sample 4..	50

Figure 20: Threshold image of sample 5 from Set 3.....	51
Figure 21: Two radiographs of Set 3 on a film viewer.	54
Figure 22: Slice from sample 7 CT data, porosity visible throughout slice.....	56
Figure 23: Slice from Figure 15 converted to binary.....	56
Figure 24: Thermographic threshold image of Set 2 sample, two different thickness	57
Figure 25: Thermographic threshold image of Set 2 sample, two areas where metal components are bonded to back surface.....	58
Figure 26: Thermographic threshold image of Set 2 sample, “edge effect” visible along length of edge.....	58
Figure 27: Thermographic threshold image of Set 2 Sample, metal inset with disbond	59
Figure 28: Set 3 radiographic film density vs porosity, linear trendline.....	61
Figure 29: Set 3 radiographic film density vs porosity, 3 rd order polynomial trendline.....	62
Figure 30: Fuji radiographic films characteristic curves [54].....	63
Figure 31: Set 3 radiographic film density vs porosity, logarithmic trendline	64
Figure 32: Set 3 thermographic t^* vs porosity	64
Figure 33: Set 3 thermal diffusivity vs porosity	66
Figure 34: Threshold image of sample 1461 with areas of varying t^* visible.....	67

Abstract

Ceramic Matrix Composites are seeing a widespread increase in use, especially in the aerospace industry. These materials are being utilized for their excellent material properties at high temperatures. As these materials are used in jet engine components and proposed as the skins of hypersonic vehicles, the consequences of material failure can be catastrophic. As-manufactured porosity is one of the earliest indicators of sub-optimal material properties that would lead to premature failure.

Non-Destructive Testing methods have long been utilized for the examination of more “traditional” composite materials. This investigation discusses the use of several NDT methods on CMCs and the advantages and limitations of those inspection methods, with a particular focus on the determination of sample porosity. Pulse-Echo Flash Thermographic Inspection is of particular focus, while Film Radiography and Computed Tomography are also examined.

Derived equations are examined for Film Radiography and Flash Thermography to determine their accuracy in calculating porosity from raw data. While Film Radiography did not yield a suitable equation, Flash Thermographic results yielded an equation which allowed for calculation of the sample porosity using only the raw data and known sample thickness. This equation was partially validated using results from additional sample sets.

The additional limitations and artifacts of Flash Thermography are examined to show the ways in which the inspection method is limited. Examinations of representative aircraft components, manufactured of CMC material, also provided realistic defects and integrated components that were located by and had varying effects on the Flash Thermographic Inspection.

Chapter 1: Introduction

This research centers around the inspection of a material class known as Ceramic Matrix Composites. These advanced composite materials have seen widespread introduction in the last several years and are expected to see a continued rise in use as global industry continues to evaluate new materials looking for the optimum solution in areas ranging from more efficient jet engines to stronger and more reliable brake discs. The inspection of these materials is essential for ensuring they are safe and reliable for use. This investigation examines some of the available non-destructive methods and practices.

1.1 Non-Destructive Testing

Non-Destructive Testing (NDT), also called Non-Destructive Evaluation (NDE), or Non-Destructive Inspection (NDI), is an overarching term encompassing many methods of examining a material. The American Society of Non-Destructive Testing (ASNT) describes the use of these methods as “the process of inspecting, testing, or evaluating materials, components or assemblies for discontinuities, or differences in characteristics without destroying the serviceability of the part or system” [1]. These methods are used to identify defects which are induced during primary or secondary manufacturing, as well as service-induced defects. ASNT regulates and certifies personnel in thirteen different methods each with sub-sets of specialized techniques, however there are many other NDT methods which are not recognized by ANST that are still used in various applications throughout the world. This research primarily focuses on ASNT-recognized thermographic testing of Ceramic Matrix Composite (CMC) materials, while also using several other methods for data validation and comparative purposes.

1.2 Composite Materials

Composite materials are materials systems “composed of a mixture or combination of two or more macroconstituents differing in form and/or material composition and that are essentially insoluble in each other” [2]. One of the basic precepts of these material systems is that the end product will have properties that are different from any one of its constituents. The goal of the material system is to use an appropriate combination of materials that yields properties optimized for the intended application of final product.

The layperson may not think of themselves as familiar with composite materials, but almost every human has seen and felt common concrete and Glass-Reinforced Plastics (GRPs) that are used in the automotive industry for body components. In the last several years Carbon Fiber Reinforced Plastics (CFRPs), another type of advanced composite that shares more in construction with ceramic matrix composites than the typical GRP or concrete, have become more prevalent in mass consumer products, such as Nike’s new Vaporfly running shoes and a growing number of bicycle frames [3, 4].

The typical advanced composite consists of two major components: the reinforcing fabric and the matrix material. The reinforcing fabric is usually a collection of many individual fibers organized into a chopped mat, unidirectional ply, or a woven ply of varying weaves. Each reinforcing fabric contributes different properties. These mats or plies will typically be layered to provide the finished component strength in the desired directions. The matrix material is initially a liquid (for CMCs this is a pre-ceramic epoxy resin) which may be impregnated into the plies either before or after they are placed into position for manufacturing. The finished product is a material which is a highly compressed set of fibers, held rigidly in place by the reinforcing matrix

material. This material can be used in an extensive and increasing portfolio of components, structural and otherwise [2, 5].

1.3 Ceramic Matrix Composites

Ceramic Matrix Composites (CMCs) are an advanced class of fiber-reinforced composites. The fibers are typically carbon- or silicon carbide-based, though other classes of ceramic fibers such as alumina-based or tungsten-carbide-based are used, and alternative fibers such as natural fibers are experiencing greater levels of research [5, 6]. As the name of CMC would imply, the matrix of these composites is a ceramic material. This can be any ceramic material ranging from those as complex as hexagonal boron nitride to simple ceramics such as common cement [5]. The CMCs that are beginning to see widespread use in aerospace environments fall towards the advanced end of the complexity spectrum.

The adoption of CMC materials in the aerospace industry is being driven by the need for materials that can withstand extremely high service temperatures while still providing an acceptable strength-to-weight ratio. The use of these materials within jet engines allows those engines to run hotter and thereby more efficiently, while their use in hypersonic vehicles allows the vehicles to travel faster with reduced thermal expansion and risk of stress damage [7, 8].

This investigation focused on a SiC/SiNC (where SiC/SiNC refers to the material of the fiber material/composite material respectively) composite known as S200, a proprietary material manufactured by COI Ceramics Inc. These S200 CMCs were manufactured using CG Nicalon™ reinforcing fibers in an amorphous SiNC matrix. Ceramic Grade (CG) Nicalon™ reinforcing fibers are manufactured from Silicon Carbide (SiC) crystallites and a mixture of silicon, carbon, and oxygen and are optimized for mechanical properties and use in high-temperature environments

[9]. The Silicon Nitride/Carbide (SiNC) matrix material enables the transfer of load to and between the fibers while also contributing its own mechanical properties. It should be noted that CMCs are classified as inverse composites due to the brittle nature of the matrix material, meaning that the matrix will fail first, and at very low strain, whereas in traditional composites, such as CFRP, the fibers fail first at low strains [5].

1.4 NDT of Composite Materials

As composite materials are used increasingly in critical structures, especially those in aerospace safety-of-flight applications, the inspection of these materials has become more important. Composite materials are inspected by many different NDT methods depending on the material composition, form, application, and type of defect anticipated. Ultrasonic testing, radiographic testing, and thermographic testing are all being utilized with varying degrees of effectiveness in detecting defects in traditional composites. Other traditional, advanced, and emerging methods of NDT not recognized by ASNT are also being used.

One of the most important factors when selecting an NDT method for the inspection of any component is understanding the defects that can be expected to occur in that component. Defect type and location is most often a function of the material, manufacturing method, and part geometry. In addition, when choosing an NDT method for real world applications other factors such as costs, inspection time, training requirements and component accessibility must be considered. However, if only defect type is to be considered for selection of the NDT methods, then Table 1 from Balageas [10] gives an excellent overview of the various methods that can be used to detect certain types of defects within a composite material. While the table is derived

originally for more traditional composites, several studies have confirmed that the data maintains validity when applied to CMCs [11, 12, 13].

Table 1: Defects detected by NDT (adapted from ASTM E2533-09) [10]

Defect	Acoustic emission	Computed tomography	Leak testing	Radiography /radioscopy	Shearography	Thermography	Ultrasound	Visual NDT
Contamination		X		X			X	X
Damaged filaments	X	X		X				
Delamination	X	X			X	X	X	X
Density variation		X		X		X	X	
Deformation under loading					X			
Disbond					X	X	X	X
Fiber disbonding	X	X ^a				X	X	
Fiber misalignment		X		X		X		
Fractures	X	X		X		X	X	X
Inclusions		X				X	X	X
Leaks	X		X				X	
Loose or moving parts	X							
Microcracks	X	X ^b		X ^{b,c}	X		X	
Moisture		X		X ^{d,e}		X		
Porosity	X	X		X		X	X	
Thickness variation		X		X ^f	X	X	X	
Undercure							X	
Voids	X	X	X	X		X	X	

^a Can detect after impact

^b Depends on opening/size of crack

^c Depends on angle of beam relative planar defect and opening

^d Only in central projection

^e Radioscopic mode

^f For radiography

The defect types most exhibited by ceramic matrix composites are delamination, density variation, disbond, inclusions, porosity, and voids [14, 11]. Table 1 shows that these six defect types are all detectable by several methods. Table 1 also shows that no method can find all the possible defect types. Both thermography and ultrasound are capable of finding all six of the most

common defect types. Thermography has been used for the investigation of CMCs with a particular focus on the determination of porosity [14]. It should be noted that even with many options for identifying defects, one of the most common methods for aerospace composite structural testing is still “tap testing” i.e., striking the composite with a solid object and listening for a change in tone.

1.5 Research Motivation

The United States Department of Defense and commercial jet engine manufacturers are exploring the use of CMCs as replacements for nickel-based super alloys for certain jet engine components that are exposed to high heat. Their goal is to reduce weight and allow for higher operating temperatures and therefore realize higher efficiency [15]. While use of these CMCs has eliminated the failure modes that were exhibited by the traditional metal components, new failure modes of delamination and loss of surface plies have been observed [16]. To maintain operational capability of the CMC components, the structural properties of the CMC materials must be at or near their ideal as-manufactured state. This means that any defects, whether service-induced or manufacturing-induced, will inhibit the ability of the component to perform as designed. Thus, it is exceptionally important to be able to inspect these CMC materials for all forms of expected defects, while balancing the need to perform the inspection in a reasonable amount of time, and find defects before they can cause harm to the component or the greater system.

Intervals for NDT are typically set based upon a calculation using the detection capability for the inspection method and the rate of known or estimated defect growth. The detection capability for a method is determined through performing Probability of Detection (PoD) studies. These studies are used to calculate the 90/95 value of that inspection, meaning that a defect of a

given size or larger will be found 90% of the time with 95% confidence [17]. Knowing the actual defect size and the defect size at which the part will fail catastrophically, along with the rate of crack growth, allows program managers to set inspection intervals with an acceptable amount of risk. The usual interval spacing is half the service time it will take for a defect of the PoD size to grow to critical size, with the intent that any given defect will be inspected twice at a detectable size before causing failure of the component [18].

When NDT fails to locate a defect, the results can be catastrophic. There have been many infamous aircraft incidents which were caused, at least in part, by NDT failing to locate a defect. In 1988 Aloha Airlines flight 243 suffered explosive decompression when a large section of the fuselage was torn from the plane while at altitude. The images of the “convertible” 737 are well known, but few know of the eddy current inspection on a repaired lap joint that was either not performed or that failed to detect the cracks that grew to critical size and caused the incident [19, 20].



Figure 1: Aloha Airlines Flight 243 [20]

Perhaps even more well-known is the crash of United Airlines flight 232 at Sioux City, Iowa in 1989 where an uncontained failure of the #2 engine destroyed the hydraulic flight controls.

The crew of that flight is often commended for their excellent Crew Resource Management and given as an example in flight schooling, but little attention is paid to the failure of the Fluorescent Penetrant Inspection process to detect a nearly half-inch long crack in a fan disk inside the engine [21, 22].



Figure 2: Failed fan disk from UA232 [22]

Even the thermographic inspection process, new to the industry as it is, has had misses leading to major incidents. In 2018 United Airlines flight 1175 suffered an uncontained engine failure over the Pacific Ocean. Fortunately, the pilots were able to guide the plane to a safe landing in Honolulu, and there were no injuries. The subsequent review of the actual thermographic inspection data from the incident blade allowed investigators to see that during the previous two inspection intervals there was an indication at the crack initiation site heralding this failure. Had the inspectors recognized this as a relevant defect and not marked the cause as “paint” it is likely the engine would not have suffered this failure [23].



Figure 3: Fractured fan blade #11 from UA1175 [23]

The need to understand the capabilities of NDT is greater than ever as the aerospace industry, in search of increased efficiency, expands its reliance on advanced materials and methods. The adoption of composite materials has given the aerospace industry a material that checks many of the boxes in the search for efficiency, but new materials must always be evaluated for new safety issues. After all, commercial aircraft cannot take passengers when they are unsafe to fly, and military effectiveness “depends, in part, on the safety and operational readiness of its [aircraft] [18].” While a great deal of research has gone into determining the capability of each NDT method’s ability to locate specific kinds of defects in traditional composites, the research into the effectiveness of those NDT on CMCs is still expanding.

1.6 Research Objectives and Investigative Approach

The research presented in this thesis is motivated to answer some of the questions about the non-destructive inspection of ceramic matrix composites. Specifically, it is geared toward the ability and effectiveness of Thermographic Inspection for use in the detection and determination of as-manufactured porosity and correlative density changes, as they can be a contributing factor in the development of several other classes of defects.

To understand the viability of thermography as an NDT method for CMC’s, all the NDT methods available to this investigation are to be examined and compared for their capabilities and limitations on the examination of CMCs.

The available and viable methods are to be utilized and the results of the inspections of the CMCs will be examined and analyzed to determine the ability, relative accuracies, and ease of use of each method in determining porosity. The results and methodologies necessary, including

required data processing, are also to be examined for their ability to provide useful data under varying conditions with and without reference standards. Thermography is also considered closely for the ability to quantitatively determine porosity in a sample using derived equations.

1.7 Thesis Organization

Chapter 2 contains information on the physics and mechanics of the non-destructive inspection methods utilized in this investigation, discussing the basics of interrogation energy and data collection methodologies. Also discussed are some historical context, basic equations, and essential terminology for the NDT methods.

Chapter 3 discusses ceramic matrix composites as a class of materials, the details of the S200 CMC which this investigation focused on, and specifics on the three sample sets which were analyzed during the course of this research effort.

Chapter 4 covers the specific manner in which each NDT method was set up and utilized to gather data including specifics about equipment. The steps taken to process and analyze the raw data from each method are also discussed.

Chapter 5 examines the results from each NDT method individually for each of the sample sets that were interrogated by that method, discussing both raw and processed data as necessary. The results are then correlated across methodologies and sample sets to determine relationships and build predictive equations from the results. The results and equations are used across the sample sets to investigate the usefulness and viability of the equations.

Chapter 6 contains final conclusions regarding the NDT methods and the results achieved towards accomplishing the research objectives. Future work for improving the results and increasing the functionality of the testing methodologies is discussed.

Chapter 2: The Science of Non-Destructive Inspection

Chapter 2 discusses the background of non-destructive testing, including some of the historical significance and unifying ideas. The physics and mechanics of the individual ASNT-recognized methods are presented including general principles, basic equations, and important terminology.

2.1 Non-Destructive Inspection Basics

While non-destructive testing is often presented as highly technical, it is a tool that is often employed in daily life. For example, checking an apple for soft spots, using a stud finder to help hang a picture, and looking for cracks in a dropped phone are all forms of NDT which correlate to industrial application of the science. Checking the apple for soft spots before ingestion is an inspection to ensure the “component” is ready for use, checking the wall for studs is inspecting the composition of the component, and looking for cracks in the phone screen is checking whether the component is likely to fail during use. Understanding the intent and basic concepts of NDT is essential to understanding the industrial applications and the advances made in the science [24].

While visual inspection is an ASNT-recognized NDT method, and likely the most widely used, it is purely reliant upon what the human eyes can pick out from the surrounding material without assistance (or limited assistance from appropriate lighting and magnification). The goal of most NDT methods is to make the sought characteristic (be that a defect in the form of a crack, a quantitative analysis of a specific material characteristic, or some other material condition) detectable or more detectable to the inspector. The genesis of NDT is most often traced back to the “Oil and Whiting” method which was developed in the late 1800’s for the inspection of railroad

train wheels [25]. Train wheels would be soaked in an oil solution, dried, and covered in a white powder. The oil would seep out of any cracks and stain the powder making the cracks much easier to see than when simply visually inspecting the wheel.

This “Oil and Whiting” method, which is the origin of the dye penetrant method, exemplifies the principle of signal-to-noise ratio (SNR). Each method of NDT will produce some form of signal during examination that is just background noise. The signal should increase when areas with an anomaly are inspected, the intensity of this increase gives the SNR. For many inspections a 3-to-1 ratio is recommended, but often the SNR of an inspection can be much higher depending on the form that the signal is taking [17]. For a fluorescent penetrant inspection where the dye in a crack is fluorescing under ultraviolet light against a nearly invisible background, the SNR (as measured by light intensity) can be several hundred to one.

While the dye penetrant method can make certain defects extremely easy to find due to the high SNR that it provides, it is not a panacea of NDT. Penetrant testing is only capable of finding surface-breaking defects, and even then, only those of a certain size and aspect ratio. Many defects which can cause issues with a material are found within the component. The multi-layered natures of fabric-matrix composites are prone to interior defects caused during the manufacture of the material, such as porosity, inclusions, and delaminations. In order to find these types of defects, an NDT method must be used that is capable of viewing the interior state of a component.

Most composite materials will be entirely opaque in the visible spectrum, rendering visual inspection capable only of finding surface-breaking defects. For visual inspection, the interrogation energy is visual light on a viewing medium consisting of the component surface. The concepts of interrogation energy and viewing mediums are readily translated to other methods of NDT. To find defects within the interior of a component, the interrogation energy must be able to

reach those defects by penetrating through the component itself. There are many forms of energy which can be used to interrogate the interior of a component; electromagnetic (both as fields and radiation), mechanical, and thermal being among the most common. Each NDT method intended to interrogate the interior of a component will make use of at least one form of penetrating interrogation energy.

The viewing medium for the interrogation energy is necessarily coupled to the type of energy being utilized and consists of two individual components: the detector and the display. The interrogation energy will interrogate the interior of a component and be changed by that interrogation. The resulting energy must be detected or recorded after the interrogation of the component. In a visual inspection this is when the light from the component hits the retina of the eye and creates an image, but for the penetrating forms of interrogating energies more specialized detectors are utilized. These can range from silver halide x-ray sensitive film for radiography to specialized sensors that measure electrical impedance in eddy current testing to mercury cadmium telluride photodetectors for infrared radiation. Once the interrogation energy has been detected it then must be displayed in a manner useful for interpretation. This is often on a digital display in the form of a graph or a representative image of the component.

When performing many NDT methods, it is commonly required to utilize what is known as a reference standard. These reference standards are most typically articles of the same material as that under investigation containing an intentional defect or even a series of defects ranging in intensity, size, or severity. These intentional defects create a reference for the investigation of the component that allows the inspector to determine what a true defect looks like, ascertain where a defect falls in a given range, calibrate equipment, or verify that the inspection method is functioning as intended [26, 17].

Four ASNT-recognized NDT methods were considered for use in this investigation, and three were selected. The three methods that were used were radiography, computed tomography, and flash thermography. Ultrasonic inspection was eliminated due to material constraints; CMCs are highly absorbent and can only be ultrasonically investigated without damage using air-coupled ultrasonics that were not available to this investigation. The three methods selected are discussed in further detail in Sections 2.2, 2.3, and 2.4.

2.2 Radiography

Radiographic Testing (RT), also known as x-ray imaging, or radiography, traces its roots to the discovery of x-rays by Wilhelm Conrad Röntgen in 1895. Röntgen discovered that by passing a large induction coil through a vacuum tube, rays were emitted, causing a barium platinocyanide screen to fluoresce. Röntgen used these “x-rays” (as he called them “for the sake of brevity”), a form of electromagnetic radiation, to investigate the ability to image through a wide variety of materials, including producing the first radiograph of the human body, a picture of his wife’s hand with bones and a ring clearly visible [27].

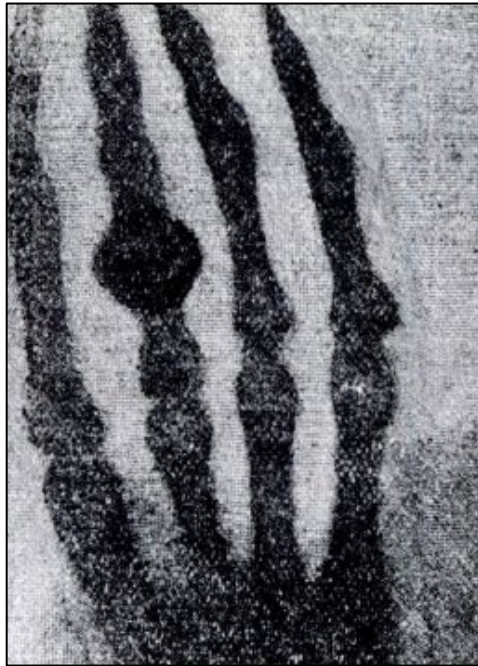


Figure 4: The first radiograph, hand of Röntgen's wife, Anna

Electromagnetic radiation is recognized for its dualistic nature, exhibiting characteristics of both particles and waves, and is most commonly characterized by wavelength (λ), frequency (ν), and energy of a photon (where a photon is the discrete energy packet of electromagnetic radiation) (E). The electromagnetic spectrum is broken up into broad “bands” by wavelengths; for example, visible light is between approximately 400 nm to 750 nm. Gamma rays and X-rays occupy the portion of the spectrum below about 10 nm [28]. X-rays and gamma rays, while they share some of the same portion of the electromagnetic spectrum, are distinct. X-rays may be produced by any of a large variety of sources (in industrial radiography x-rays are produced by specific generation equipment using the impact of high energy electrons with matter) whereas gamma rays are produced solely by the decay of radioactive material and will typically have a higher energy than that of industrially-produced x-rays. The wavelengths and energies of electromagnetic radiation are related by the equation:

$$E = \frac{1.24}{\lambda} \quad [1]$$

where E is given in keV and λ is given in nanometers [29]. Electromagnetic radiation with enough energy to be part of the x-ray or gamma ray spectrum is known as ionizing radiation. Ionizing radiation is that radiation capable of removing bound electrons from atomic shells. In human tissue, this ionization can lead to damage of our biological material making exposure extremely dangerous [29].

Using ionizing radiation is essential to creating an image of the interior of an object with the radiographic method because the ways that radiation will interact with matter can be more representative of either the wave-like or particle-like nature of electromagnetic radiation depending on the energy of the radiation relative to the size of the object being struck by the radiation. Visible light interacts in a way that exhibits the wave-like nature: being absorbed, diffracted, or refracted and thereby shifting wavelengths to present colors to our eyes. The much higher energies and shorter wavelengths of x-rays lead to the photons interacting with matter in a more particle-like behavior. The photons of the x-rays will penetrate through the matter of an object and interact with individual sub-atomic particles. These particle-like interactions happen in three main categories.

The first of these categories is that the photon will pass through the matter without interacting with any atom of that matter. The second category of photon-matter interaction is scattering. There are two types of scattering: Rayleigh and Compton. Rayleigh scattering occurs mainly with very low energy photons and accounts for a very low percent of the total interactions between photons and matter in industrial radiography. Compton scattering is the predominant interaction between photons and matter at the high energies of industrial radiography. During Compton scattering a photon strikes an atom which results in an ejection from that atom of a lower

energy photon (which also changes angle of incidence) and a secondarily ejected electron (which ionizes that atom, hence ionizing radiation). The secondarily ejected electron may then pass through the medium in whichever direction it was ejected or have secondary interactions within the matter. The third category of photon-matter interaction is absorption. The photons are absorbed in two different manners, through the photoelectric effect or pair production. As pair production only occurs at extremely high energy levels (above 1.02 MeV), industrial radiography is dominated by the photoelectric effect. In the photoelectric effect all of the energy of an incident photon is transferred to an electron that is ejected from the atom (again ionizing that atom) [29].

When a beam of x-rays is directed at matter, it is attenuated where attenuation is defined as the “removal of photons from a beam of x-rays... as it passes through matter” [29]. This attenuation is caused by the absorption and scattering mechanisms described above. The rate of attenuation for a material being struck by photons of a given energy is described by a form of the Beer-Lambert Law:

$$N = N_0 e^{-\mu x} \quad [2]$$

where N is the number of photons transmitted through an object, N_0 is the number of photons which were incident upon that object, μ is the linear attenuation coefficient, and x is the thickness of the object through which the photons were transiting [29].

The linear attenuation coefficient is based upon several material properties including density, electrons per mass, and electron density and will vary based upon the energy of the incident radiation. In a composite material such as CMCs, the exact determination of this coefficient analytically can be extremely complex, though it increases approximately by the element’s z-number (the atomic number of that element on the period table) in accordance with the rule of mixtures [30]. While empirical determination of μ is not as difficult, knowledge of the

exact attenuation is not necessary for the creation of useful radiographs, as the data gathered by radiographs is typically comparative and not examined in an absolute manner.

The radiation that does penetrate fully through an object must be detected to create a functionally useful radiograph. There have been many forms of x-ray detectors used in the century and a half since Wilhelm Röntgen first used a barium platinocyanide fluorescent screen to investigate radiation. For much of that time the standard medium of detection was film, originally standard photographic film until x-ray specific film was developed. In recent years however, digital detectors have nearly eliminated the use of film, especially in the medical industry. Detectors are usually made of high a z-number material to ensure that the maximum number of interactions can take place [31].

The creation of a radiograph, despite the complex physics upon which the method is based, is a relatively simple process. The object of interest is placed between an x-ray source and the detector. X-rays are generated and are differentially attenuated through the object of interest before striking the detector. As the object varies in attenuation across the plane of interrogation, that variance will be recorded by the detector. This creates a 2-Dimensional image of the object which is representative of the attenuation through the object in a given direction. As the attenuation is correlated with the thickness of the object and the attenuation coefficient of the material through which the radiation is traveling, it is possible to see variations in thickness, material, or density across and through the object of interest, including some of the defect types possibly in CMCs [31].

2.3 Computed Tomography

As discussed previously, traditional radiography provides an image through the thickness of an object in one direction. While this can provide very useful information about relative material density through an area of an object, there is no information on the depth of any features visible on that radiograph. For example, in the radiograph shown in Figure 5, the bright spots indicate areas or inclusions of a more attenuating (likely higher density) material somewhere through the thickness of the object being examined. Unfortunately, this gives no indication of where the inclusion might be through the thickness. Computed Tomography (CT), colloquially known as a “cat scan,” is an inspection method which gives three-dimensional data about an object by expanding on the inspection principles of traditional radiography.



Figure 5: Radiographic image of a weld with inclusions (bright spots) [55]

While traditional radiography creates a two-dimensional image for each exposure, computed tomography creates a three-dimensional image essentially by combining many one-dimensional radiographs, taken from many angles surrounding an object, and combining them algorithmically, then repeating this process for many “slices” as the object is translated through the imaging area.

To gather the attenuation data, when performing a CT scan the incident radiation is estimated at the source by the power output of the x-ray generating tube head and then detected after it has passed through the imaged object. As the distance between source and detector is set by the design of the imaging equipment, this gives all the parameters necessary to calculate the linear attenuation coefficient of the object using Equation 2, in the scanned line (included in the calculation is the attenuation of the air on either side of the scanned object, though this has minimal effect). The linear attenuation coefficient is then normalized against the linear attenuation coefficient of water using Equation 3, which gives the CT number or Hounsfield Unit [31, 29]. This CT number is the displayed parameter (through pixel/voxel intensity) when viewing a CT scan image [31].

$$CT\ Number = 1000 * (\mu - \mu_{water}) / \mu_{water} \quad [3]$$

A CT scan will give raw data of the CT number of the scanned object at many angles, however this is not immediately useful data and can be visualized as many overlapping lines of a single data point, as shown in Figure 6.

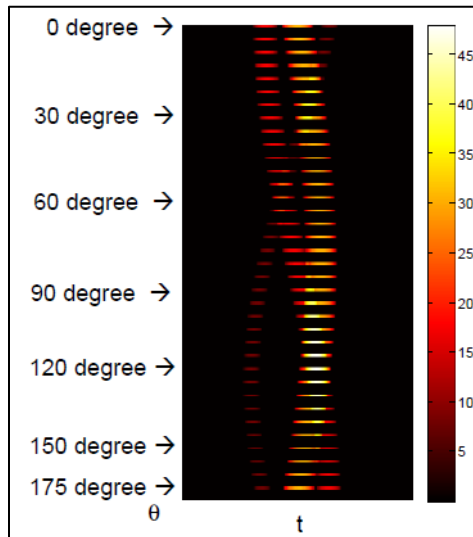


Figure 6: Visual representation of CT data [31]

The conversion of this linear data into discrete data points can be done algebraically, however when the images consist of several hundred or thousand data points through the area of interest these calculations become extremely computationally intensive. Modern calculations use Fourier transforms to create a two-dimensional image for each slice. These slices are stacked and create a single three-dimensional image of the object with discrete data points throughout the interior of the object [31].

2.4 Flash Thermography

Thermography as a general NDT method is the determination of the temperature of a point or surface. Temperature determination can be indicative of a variety of factors, especially when observed during use of the object being investigated. As such, thermography is primarily used for the investigation of home utilities and predictive maintenance of motors, electrical lines, and other equipment [32]. However, for specimens at rest a simple temperature determination is not sufficient to determine anything about that the condition of that specimen. The sample must be imparted with external interrogation energy, which can be of several forms, most commonly electromagnetic, thermal, or mechanical.

For flash thermography the interrogation energy is electromagnetic radiation created via a set of flashbulbs which produce a very energetic and brief burst of radiation that can be seen as visible light as it strikes the exposed surface of the object under investigation. What humans think of as light is simply electromagnetic radiation within the “visible” range of the spectrum which is approximately 400 nm to 750 nm and is only part of the thermal radiation portion of the electromagnetic spectrum which extends from about 100 nm to 100,000 nm and includes infrared, visible, and some ultraviolet radiation [33]. Much of the thermal energy used to interrogate the

sample falls within the infrared range, which is not visible to the human eye, but still carries most of the energy from the flash bulbs to the component [34]. Special cameras with detectors designed to detect specific portions of this “invisible” radiation are used for thermographic inspections [32].

For infrared radiation the principles of absorptivity, reflectivity, and transmissivity are much more important. This is because infrared radiation is of an energy much lower than the x-ray and gamma rays discussed in Section 2.2 where a vast majority of the radiation penetrates through the interrogated object to some extent. Absorptivity, α , is the fraction of incident radiation which is absorbed by the surface of the object, reflectivity, ρ , is the fraction which is reflected by the surface, and transmissivity, τ , is the fraction that is transmitted through the surface [35].

$$\alpha + \rho + \tau = 1 \quad [4]$$

As can be seen in Equation 4 these three factors account for the total of the radiation which is incident on the surface of an object. For the idealized “blackbody” $\tau = \rho = 0$ and all the radiation incident on the body is absorbed, however this is never the case for any real object, since all real objects have some level of reflectivity, transmissivity, or a combination of the two [35]. While most solid objects do have a transmissivity of zero (or nearly so, meaning that the entirety of the absorbed and reflected energy interacts within a layer which can be approximated as infinitely thin at the surface of the object), CMCs exhibit a small amount of transmissivity in the infrared spectrum (though not the visible spectrum).

The energy of the electromagnetic generated by the flash bulbs during flash thermography strikes the surface of the object under investigation where most of the energy is absorbed in accordance with the relatively high (~ 0.95 in the infrared spectrum) absorptivity of CMCs. As the energy striking the object falls mostly within the visible and infrared wavelengths of the electromagnetic spectrum it is absorbed almost entirely very near the top surface of the object,

though not entirely at the surface layer due to the slight transmissivity of CMCs in the infrared spectrum. For flash thermographic inspection, the specimen should be at thermal equilibrium throughout the specimen volume as well as with the surrounding environment before the energy is imparted onto the top surface of the specimen. The absorbed incident radiation is converted into thermal energy creating a thin “hot” layer at that surface when compared to the thermal state of the rest of the object.

The second law of thermodynamics gives that the heat in the top layer of the specimen will seek equilibrium with the rest of the system, including the rest of the specimen and the air around it [36]. The system will seek thermal equilibrium through the three modes of heat transfer: convection, conduction, and radiation. While conduction and radiation both play an important role in flash thermography, convection only removes thermal energy from the system in a manner which does not contribute to the investigation and can decrease the accuracy of the results if too much energy is removed; consequently, it is necessary to minimize convection during flash thermography.

The effects of convective heat transfer are minimized through several factors. Natural convection, which relies upon the buoyancy effects of heated gasses, is minimized due to the relatively low temperature difference between the heated specimen and the surrounding air. Forced convection is minimized simply by the setup of the experiment, which is typically performed in a controlled or enclosed environment that prevents all external convection.

Unlike convection, conduction plays an important role in the process of flash thermographic inspection. Conduction is “the transfer of energy from the more energetic particles of a substance to the adjacent less energetic ones as a result of interaction between particles” [36] and is the primary mode of thermal energy transport within a solid material where conduction is

caused by a temperature gradient through that material [37]. The equation for one-dimensional steady state heat conduction as first published by J. B. Fourier in 1822 best shows the factors which contribute to heat conduction through an object [38]:

$$q'' = k \frac{T_1 - T_2}{L} \quad [5]$$

where q'' is the heat flux through the object (SI unit: W/m^2), k is the conductive heat transfer coefficient, T_1 is the temperature of the “hot” surface, T_2 is the temperature of the “cold” surface, and L is the distance between the two surfaces. As can be determined from this equation there are essentially two factors that contribute to the heat flux through an object: the driving force and the conductive heat transfer coefficient. The temperature difference across the object provides the “driving force” of the heat conduction through the object and is a factor solely of the setup of the heat transfer. The conductive heat transfer coefficient is a material property that can be isotropic or anisotropic, especially in composite materials where the individually oriented fiber components may have different heat transfer coefficients from the matrix in which they are embedded [37].

During flash thermography only the top surface of the sample is heated through the processes described above providing a temperature gradient across the specimen from the heated top surface to the pre-flash-equilibrium temperature bottom surface (and indeed, immediately after the initial flash, all of the specimen apart from the heated top surface is the same pre-flash equilibrium temperature). The heat which is absorbed at the top surface during the flash, apart from providing the driving force for conduction, is the entirety of the thermal energy that is conducted through the specimen during the thermographic inspection. The specific manner in which the heat is conducted through the sample is discussed later in this section, however as a general rule the heat will be conducted through the sample in a relatively even “wave” towards the bottom plane of the specimen.

One of the limitations of the Fourier equation for heat conduction is the way in which it handles “speed” of conduction; the Fourier equation implies that any change will be felt instantly throughout a material, which is faster than the speed of light and therefore impossible. Clearly some amount of time is required for any change in thermal energy to be conductively diffused through an object, though the determination of this speed is extremely complex. One of the equations that attempts to account for the speed of heat conduction is the Maxwell-Cattaneo law:

$$(1 + \tau_0 \partial_t) \mathbf{q} = -k \nabla T \quad [6]$$

which includes the thermal relaxation time, τ_0 , with the partial time derivative, ∂_t , creating a time dependent conduction equation, where \mathbf{q} is the thermal flux vector, k is the thermal conductivity, and ∇T is the temperature gradient [39, 40]. This law can be used to model an approximate finite speed of thermal propagation, v [41]:

$$v = \sqrt{\alpha / \tau_0} \quad [7]$$

which introduces the important concept of thermal diffusivity that is often viewed as representing the ratio of heat conducted through a material to the heat stored per unit volume in that material [35]:

$$\alpha = \frac{k}{\rho c_p} \quad [8]$$

where ρ is the density and c_p is the specific heat capacity of the material.

The equation for thermal diffusivity is derived from the combined heat equation for energy conservation ($E_{in} - E_{out} + E_{generated} = E_{stored}$) within a 1-Dimensional system, shown below [37]:

$$\frac{\partial}{\partial x} \left(k \frac{\partial T}{\partial x} \right) + \dot{q} = \frac{\partial (\rho C_p T)}{\partial t} \quad [9]$$

In this equation, the net heat conduction term is a reorganization of Equation 5. When k , ρ , and c_p are treated as constant, and \dot{q} is zero (as is the case in this investigation) this equation simplifies to:

$$\frac{\partial^2 T}{\partial x^2} = \frac{\rho C_p}{k} \frac{\partial T}{\partial t} \quad [10]$$

utilizing Equation 8's value for thermal diffusivity.

This investigation does not provide nor rely upon mathematical calculations of thermal diffusivity for the CMC materials based upon material properties, however empirical calculations of thermal diffusivity are an essential component of the correlations provided later for determination of sample porosity from thermographic results.

The conductive heat coefficient in a homogenous material does not change throughout the specimen or with the changing temperatures present in flash thermographic investigation (the absolute temperature differences used in flash thermography are not large enough for most temperature dependent conductive heat coefficients to vary significantly) [38]. When there is a discontinuity within the material there is almost always a change in heat conduction coefficient due to that discontinuity.

As discussed in the introduction, the failure modes of concern for this investigation were delamination, density variation, disbonds, inclusions, porosity, and voids. Inclusions are simply the presence of a foreign material within the specimen of interest. These inclusions can be of any material with their own corresponding thermal conductivity, higher or lower than that of the base specimen. Delaminations, density variation (which in CMCs is caused by unfilled internal porosity/pores), disbonds, porosity, and voids all present with at least some small amount of internal volume being filled only by trapped air or off-gasses from the sample itself. While heat transfer in fluids is usually dominated by convection, volumes of gas with diameters less than 4

mm do not experience this convection, leaving conduction as the dominant form of heat transfer [42]. It is important to note that these gasses will, in most cases, have a thermal conductivity that is several orders of magnitude lower than that of a solid material by in which they are found. S200 CMC's have a thermal conductivity of approximately 2.1 W/m*K while gasses typically range from 0.015-0.030 W/m*K with air being 0.0252 W/m*K at room temperature [43, 44]. The localized changes in thermal conductivity created by any of these defects have a profound effect on heat conduction through the specimen under investigation. While this investigation does not perform calculations of theoretical thermal conductivity, the equation given by Maxwell gives thermal conductivity for a material containing embedded spheres of small volume fractions:

$$\frac{k_{eff}}{k_0} = 1 + \frac{3\phi}{\left(\frac{k_1 + 2k_0}{k_1 - k_0}\right) - \phi} \quad [11]$$

where k_{eff} is the effective thermal conductivity of the material, k_0 is the initial thermal conductivity of the material, k_1 is the thermal conductivity of the small spheres (porosity in the composites application), and ϕ is the volume fraction [38].

After the initial pulse of electromagnetic energy, the final mode of thermal energy transfer, radiation, transfers only a tiny amount of thermal energy in flash thermography. However, radiation plays a very important role providing the viewing energy for the investigation. By Planck's Law it is known that "a body at a thermodynamic (or absolute) temperature above zero emits radiation in all directions" and the mathematics of Planck's Law show that as the temperature of the body increases, the total amount of energy radiated will increase [35]. This energy is emitted in a curve over a range of wavelengths. As Planck's Law goes on to state, the total energy radiated by a body increases as the peak of the emitted spectrum moves to a shorter wavelength. The shifting of the spectrum to shorter wavelengths is described by Wien's displacement law:

$$\lambda_{\max power} = \frac{2897.8}{T} \quad [12]$$

which gives the radiation wavelength of maximum power for a black body of a given temperature in μm [35]. For an object at room temperature (298K) Wien's displacement law gives a wavelength of $9.72 \mu m$, firmly within the infrared portion of the electromagnetic spectrum which ranges from $0.74 \mu m$ to 1 mm [35, 28]. During flash thermographic inspection the surface of the object being investigated will change temperatures over time and at different rates across the surface. The specific NDT technique used by this investigation is known as "Pulse-Echo" flash thermography where the investigated surface is the same top surface which receives the thermal energy from the flash bulbs. Other flash thermographic inspection techniques include "through-transmission" where the thermal energy is detected on the opposing surface from where the thermal energy is imparted. In accordance with Planck's law each point of the examined surface will be continuously emitting radiation and by Wien's Law this radiation will peak at different wavelengths dependent upon temperature. The observation of this radiation can be used to calculate surface temperatures which are then displayed as the raw data for flash thermographic investigation.

During investigation the top surface of a flash thermographic specimen will cool from the initial "heat" of the flash pulse until it reaches an equilibrium temperature where all the thermal energy imparted by the flash is spread evenly through the specimen. The top surface temperature for a thermographic inspection of an infinitely thick slab is governed by the equation:

$$\Delta T = \frac{Q}{e\sqrt{\pi t}} \quad [13]$$

where ΔT is the temperature change relative to the pre-excitation state, Q is the absorbed energy, e is the thermal effusivity, and t is the time where the initial flash is $t=0$ [45]. Regardless of the material used, when ΔT is plotted vs time on logarithmic scales the result is a line with slope -0.5 as seen in Figure 7 [45].

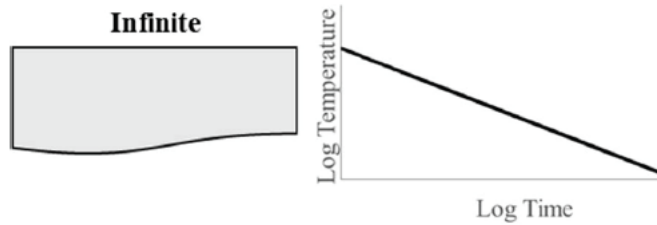


Figure 7: Heat conduction through an infinite slab, log surface temp vs log time [45]

When the heat is not conducted through a slab of infinite thickness and rather a more realistic object with an adiabatically insulated bottom surface, the resulting plot, as seen in Figure 8, initially displays the same -0.5 slope but when the initial wave of heat reaches the insulated surface, the slope transitions to a horizontal line.

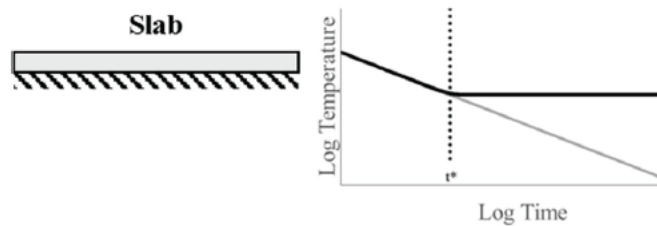


Figure 8: Heat conduction through material with insulated bottom surface, log surface temp vs log time [45]

Where the asymptotes of the -0.5 slope line and the horizontal line cross a time, t^* , is found. The t^* represents the time at which the thermal energy has reached the back surface of the specimen and can be related to the material physical properties by the equation:

$$t^* = \frac{T^2}{\pi\alpha} \quad [14]$$

where T is the thickness of the specimen [45]. This measurement of t^* is essential for characterizing the investigated material. As the measurements of thickness and t^* can both be determined experimentally, this equation can be used to determine the thermal diffusivity of the specimen.

When the thermal energy that is being conducted through a material reaches an inclusion of different thermal conductivity, the temperature, measured at the top surface will change at a rate different from the consistent rate of conduction through the base material. A material which is more insulative, having a lower rate of thermal conductivity or diffusivity, will appear to deflect above the baseline -0.5 rate while a material which is more conductive will appear to deflect below the baseline. Figure 9 shows graphs where the plotted lines show the behavior of top surface temperature for conduction through the base material into a material of different conductive properties [45].

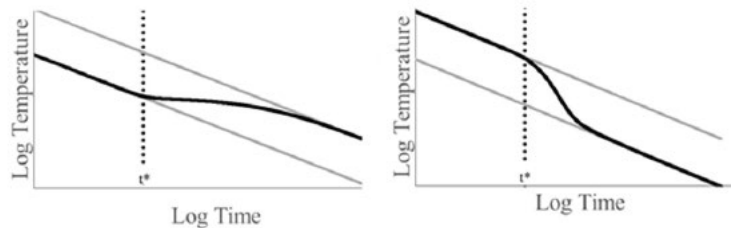


Figure 9: Log surface temp vs log time graphs for inclusions of lower (left) and higher (right) conductivity [45]

The graphs in Figure 9 are presented for a flat panel of baseline material abutted to an infinite panel of the material of different conductive properties; as the thermal energy moves into the second material the rate of thermal conduction stabilizes on the -0.5 rate.

When thermal energy is imparted to a homogenous specimen during flash thermography the energy moves at a consistent rate through the specimen in all directions (ignoring edge effects),

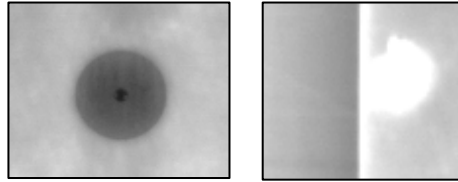


Figure 10: Defects in CMCs as thermographically imaged, metal inclusion (left) and disbond (right)

away from the surface which received the electromagnetic energy creating a “wave” of energy. However, when the “wave” reaches an area of varying thermal diffusivity (a defect), the energy transfer will change “speeds” creating localized areas within the wave of greater or lesser thermal energy. The thermal energy around these differing areas will not only progress through the component as the energy attempts to reach equilibrium through the thickness of the component but will also attempt to reach equilibrium with the differing area within the wave created by the defect. As the consequences of the thermal energy transport can be viewed as changes in temperature on the top surface, these defects will be apparent on the top surface, roughly in the shape of the defect, though with slightly undefined edges. Like the infinite planes explained above, a defect which reduces the thermal diffusivity of an area will appear as an area on the surface where the thermal energy reduces more slowly and is consequently “hotter” than the surrounding areas, and a defect which increases the thermal diffusivity will appear “cooler” than the surrounding areas. In Figure 10 the images from Set 2 show an area where a metal insert has increased the thermal diffusivity and an area at the edge of the component where the plies have become disbanded, reducing the thermal diffusivity.

Non-homogenous materials, including fiber-composite materials, often display anisotropic thermal properties. This can pose an additional challenge for detection of defects using flash thermography as the thermal energy may be diffused laterally, along the fibers, throughout a

specimen at a faster rate than the conduction of the energy through the thickness of the specimen. This differential rate of thermal energy transport can mask defects as the energy is moved into or away from the areas of differing energy levels created by those defects too quickly to detect. Materials which are homogenous but have extremely high thermal conductivities, such as most metals, are also extremely difficult to test using flash thermography as the thermal energy is transported too rapidly for adequate defect detection. Equally damaging to the inspection capability of flash thermography are defects which are too small or too deep for the thermal energy disruption on the top surface to be detected. In addition, specimens that are too thick may not provide adequate inspection results of the total thickness. However, despite these and other restrictions, flash thermography is an extremely capable tool for inspections of appropriate materials and can be leveraged to replace or supplement more expensive and time-consuming inspection methods in many applications.

Chapter 2 discussed the science of NDT and of each ASNT-recognized NDT method that was utilized in this investigation, as well as some of the history, basic equations, and important terminology. The next chapter discusses the samples that these methods were used on throughout the investigation, including the basics of CMCs, S200 material specifics, and the individual sample sets.

Chapter 3: Ceramic Matrix Composites and Samples

Chapter 3 discusses ceramic matrix composites as a class of materials, their usage, and manufacturing. The S200 material that this investigation focuses upon is discussed in greater detail, as are the sample sets that this material is used in. This serves as a basis for understanding the types of defects which occur, why they are important, and how NDT might be useful for locating them.

3.1 Ceramic Matrix Composites

The goal of any composite material is to create a material that has a combination of properties that are different than any of its constituent materials. The choice of materials used, the forms in which they are integrated, and the manufacturing process utilized can create a composite material that has been optimized to provide improved properties such as strength, stiffness, corrosion resistance, wear resistance, various thermal and temperature dependent properties, longer fatigue life, or greater toughness [2]. Traditional ceramic materials often have excellent thermal properties but are typically extremely brittle and therefore unsuitable for use in structural applications [46]. A composite based upon ceramics could improve upon the low toughness of traditional ceramics while retaining much of the excellent thermal properties.

Ceramic Matrix Composites (CMCs) were first investigated nearly 60 years ago in the development of high temperature materials for the nascent space industry [47]. As the manufacturability of CMCs has improved, CMCs have been adopted in industries far beyond space applications culminating in the debut of the CFM International LEAP Jet Engine, which became the first product incorporating CMCs to see widespread commercial use when it debuted in 2016

[48]. The driving force behind the growing use of CMCs is the increasing need for materials which can withstand both high levels of stress and extremely high temperatures. In jet engines, CMCs can replace hot section components which typically must be made of heavy superalloy metals, reducing weight and cooling requirements thereby helping increase efficiency of the engine [49]. Formula 1 race cars and high-end sports cars are available with CMC brake discs that have better wear and braking performance at high temperatures than their steel counterparts while providing a longer usable lifetime [49]. Other current CMC usage includes body armor for soldiers and policemen, bearings in petrochemical pumps, and gas turbine components, while scientists are currently exploring possibilities for use in Generation IV nuclear plants and hypersonic flight vehicles [48, 49].

3.2 S200 Ceramic Matrix Composite Material

Three sets of specimens, all of different forms, fits, and functions, were used during this investigation to understand the ways in which the NDT methods would assess CMCs. All were manufactured of a CMC developed by COI Ceramics Inc. known as S200. This CMC is known as a SiC/SiNC composite, being composed of Silicon Carbide (SiC) fibers contained within a Silicon Nitride/Carbide (SiNC) matrix material [50].

The SiC fibers are Ceramic Grade (CG) Nicalon™ fibers that are manufactured by the Nippon Carbon Co. and composed of “ultra-fine beta-SiC crystallites and an amorphous mixture of silicon, carbon, and oxygen” [9]. These fibers can be utilized in polymer, metal and ceramic matrix composites and will provide high strength and modulus even at high temperatures as well as exhibiting excellent resistance to oxidation and chemical attack. Nicalon™ fibers come in a

variety of forms including continuous or chopped fibers, woven cloth, and felt [9]. All of the components in this investigation were manufactured using various weaves of cloth.

The SiNC matrix material gives the composite its stiffness in the transverse orientation to the fibers, as well as enabling the transfer of load to and between the fibers. It is important to note that CMCs are classified as inverse composites due to the brittle nature of the matrix material, meaning that the matrix will fail first, and at very low strain, whereas traditional composites, such as CFRP, will see the fibers fail first at lower strains [49]. This nature of CMCs drives the desire to eliminate or reduce cracking initiation sites, such as internal porosity, as cracks will substantially weaken the material, proportionally more than in a traditional composite [49].

The six primary defect types found in composites, including CMCs, are discussed in Section 1.4. They are delamination, density variation, disbond, inclusions, porosity, and voids. This investigation focuses primarily on the detection of porosity as when a CMC contains a high level of porosity it becomes more severely “vulnerable to strength degradation and damage upon prolonged exposure to service loads and environmental conditions” [14]. Porosity within CMCs is a defect seen in the as-produced condition, i.e. new from the manufacturer, and as such is a primary manufacturing defect or a failure within the manufacturing process.

While there are several major manufacturing processes used in the production of CMCs including Chemical Vapor Infiltration (CVI) and Melt Infiltration (MI), all of the components used in this investigation were manufactured using a process known as Polymer Infiltration and Pyrolysis (PIP). The PIP process begins in a manner which is very similar to traditional polymer matrix composite manufacturing; the ceramic fiber fabric or tow to be utilized is impregnated with a special pre-ceramic polymer to form a what is known as a “prepreg.” These prepreg cloth layers are stacked, typically in a mold, and then consolidated using an autoclave or press. Once the

polymer has cured, the “green-state” component can be removed from the tooling and will theoretically be 100% dense with no incorporated voids [51].

The initial polymeric matrix of the green-state component must be converted to a ceramic matrix to create a complete ceramic matrix composite. This conversion is performed through pyrolysis, a process in which the component is heated to temperatures above 850°C, sometimes up to 1,400°C, in an environment of argon, nitrogen or ammonia [51, 8]. As the matrix goes through the conversion from polymer to ceramic, the matrix material experiences substantial shrinkage and weight loss resulting in the component having a void content of 20-30% after initial pyrolysis. To increase the density, the component is reimpregnated with pre-ceramic polymer resin. The component is then subjected to an additional pyrolysis cycle to convert this newly infiltrated polymer to ceramic matrix material. The PIP cycle is usually repeated several times and can be used to precisely control the density of a finished CMC component. Figure 11 shows how increasing PIP cycles affect component density [51].

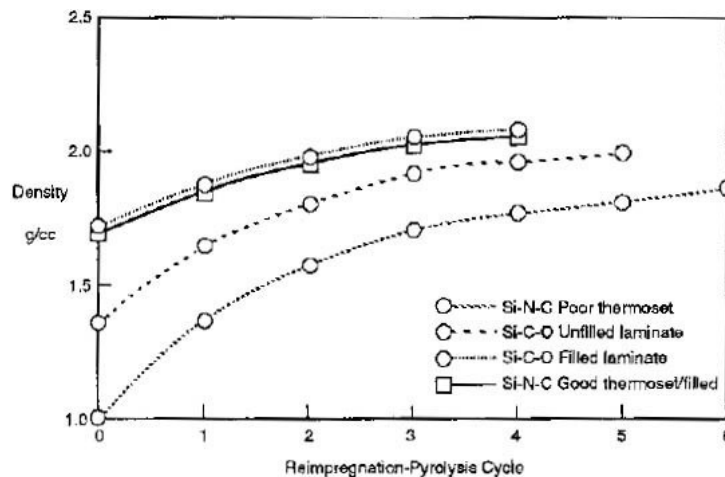


Figure 11: Effects on density of increasing PIP cycles for CMCs of various matrix materials [51]

While repeated PIP cycles will increase the density of a CMC by filling open pores in the material with ceramic matrix material, some porosity can become closed to infiltrating resin [52]. When this occurs, those pores may never be able to be filled with matrix material and will remain, regardless of the number of PIP processing cycles. The porosity is generally randomly distributed; however, it may be found in higher concentrations near the center of the manufactured component.

3.3 Sample Sets

Three sets of components were procured for this experiment which cover an extensive range of designs, interfaces, sizes, and use cases. As stated in Section 3.2, all the sample sets were manufactured of S200 CMC material using the PIP process. These three sample sets are referred to as Set 1 or “Large Plates,” Set 2 or “Representative Aircraft Components,” and Set 3 or “Porosity Coupon Sets” and are discussed in individual detail below.

These three sets were chosen primarily because of their availability to this investigation as samples of the same material type, with additional considerations of set diversity and utility for investigative information. The sample sets were provided with varying levels of background information including porosity volume fraction for Sets 1 & 3, and additional background density data for Set 3. The investigative methods that each set was subjected to are discussed in Section 4.1, though in general each set was investigated by the available and suitable methods that would yield functional data. Sets 1 & 3, being nearly uniform samples, were investigated in their entirety. As discussed in Section 5.4, Set 2 had several specific areas of interest due to the complex nature of the components, which received additional attention.

3.3.1 Set 1: Large Plates

Set 1 is a set of two 18"x18"x0.25" square panels. Each of these plates contain two 0.125" diameter copper rods which are insulated from the surrounding CMC and pierce through approximately 75% of the plate thickness. The plates represent two average porosities of 8% and 22% for samples 1450 and 1461 respectively (as determined by Archimedes performed by UDRI). These samples were provided by the University of Dayton Research Institute (UDRI) in coordination with the Air Force Research Laboratory (AFRL).

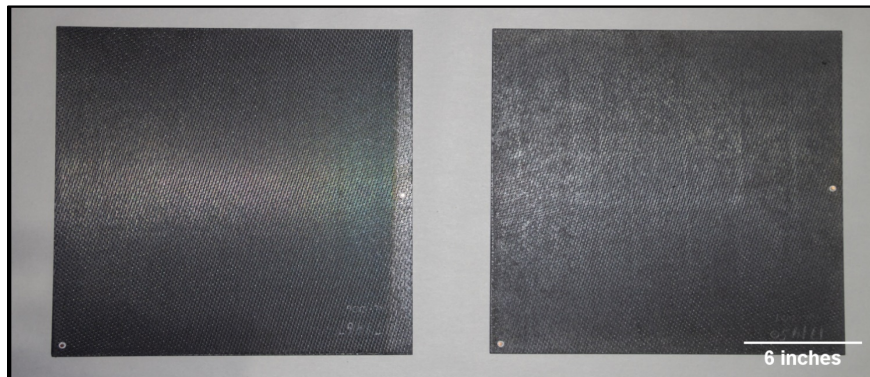


Figure 12: Samples 1450 (right) and 1461 (left) of Set 1

3.3.2 Set 2: Representative Aircraft Components

Four test components were provided by a program office of the Department of Defense. These components represent the most realistic usage of this material in terms of how it would be integrated into a production aircraft component. These specimens contain design elements that include thickness variations, curvatures, and the integration of significant metallic structures. In addition to the design elements, these components also contain service-induced defects which were not apparent by initial visual investigation but became apparent during the experiment's investigations. While no porosity changes were seen through these components, they did provide an excellent perspective of the expected conditions for CMC components.

3.3.3 Set 3: Porosity Coupon Set

The Porosity Coupon set was provided by COI Ceramics Inc. and represented the largest and most controlled sample set utilized in this investigation. The set consisted of 10 panels (numbered 2-11) that are 2.5” x 4” with a thickness of approximately 0.27”. The samples covered a range of porosities from <2% to >20% with no additional inserts or inclusions. The broad range of porosities, with small and regular intervals, created an ideal set to gather data for a comparison of porosities in an otherwise controlled group. This controlled set can also act as an ideal NDT reference standard for the relative comparison of porosities.

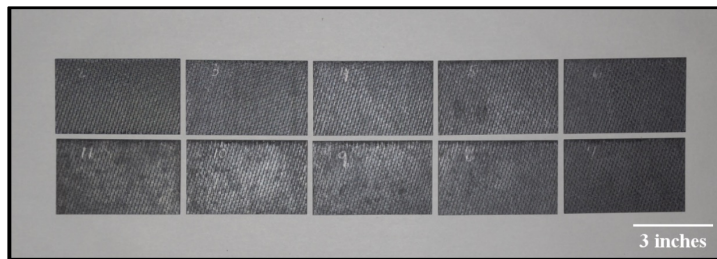


Figure 13: Samples from Set 3 arranged by decreasing porosity, clockwise from top left

Traditional NDT ideology would indicate that this reference standard would only apply to CMC samples of the same thickness and material, however one of the interests of this investigation is to use the analysis of Set 3, as well as that of Sets 1 and 2, to determine if the usage of Set 3 as a reference standard can extend beyond those limitations.

This investigation utilized sixteen samples spread across three sets consisting of Large Plates, Representative Aircraft Components, and the Porosity Coupon Set. These samples represent a range of porosities, thicknesses, and geometries, which provide useful features for

determining the viability of the NDT methods to which they were subjected. The testing and data processing methodologies used on these samples are discussed in Chapter 4.

Chapter 4: Testing & Data Processing Methodology

Chapter 4 discusses the testing methodologies utilized by this investigation for their particular use and set up on the CMC samples. This discussion also covers the ways in which each method provided raw data and how that raw data was processed into a functional form for analytical purposes.

4.1 Testing Methods & Data Processing

Samples from each of the three sets were subjected to various methods of interrogation to determine properties of those samples. The methods of interrogation were chosen for the data gathered by that method, the availability of that method to this investigation, and the impact of the method on the samples. Each of these methods gave data of a different type and often required additional processing before analysis.

In this section, each of the four methods used to gather data for this investigation, Archimedes and the three NDT methods of radiography, computed tomography, and flash thermography, are discussed for how they were utilized. The sample set that each method was used on is shown in Table 2. For each of these methods a discussion of the data gathered and any necessary processing for analysis is included.

Table 2: NDT methods used by sample set

	Set 1	Set 2	Set 3
Archimedes	X		X
Radiography			X
CT			X
Thermography	X	X	X

4.2 The Archimedes Method

The Archimedes method is the oldest and simplest method of determining the density of an object. The object is weighed using a sensitive scale to determine mass. The object is then immersed in a fluid to determine volume by displacement. The measurements of mass, m , and volume, v , are the only inputs necessary to calculate density, ρ , using Equation 15 [33].

$$\rho = m/v \quad [15]$$

For CMC samples, Archimedes is the most common method of density determination, but the volume determination can be somewhat difficult. Many CMCs, including the S200 examined in this study, will absorb moisture into the matrix of the material if the exposure to liquid is prolonged or even if the relative humidity is too high. Additionally, the most common defect, porosity, both open and closed, can cause issues with this simple calculation. Porosity open to the infiltration of the fluid may or may not be included as part of the volume of the component depending on how the sample is immersed and the surface energy of the component. Samples in which the porosity is not homogenous will average to the calculated density but if local density measurements are taken these will likely differ from the sample average.

4.3 Radiography

Radiographic imaging provides comparative data of relative x-ray attenuation of the imaged object. To gather accurate data from separate images, those images must be taken using the same amperage, voltage, distance, and film speeds. The differential attenuation across objects is extracted into empirical data from x-ray images using different techniques based upon the type of detector used to gather the x-ray energy.

Images collected using a digital or computed radiographic method can be examined using specialized radiographic image analysis software. The radiographic data is typically presented graphically in a 16-bit depth grayscale representation of the detected radiation. This software can provide information of how much x-ray energy was detected for any specific pixel or region of pixels in a radiographic image.

The resources available to this investigation were only able to produce images on silver bromide emulsion-based film, commonly known as “wet film.” This emulsion is photosensitive to electromagnetic radiation and as such forms a latent image in accordance with the Gurney-Mott concept of exposure when the x-ray radiation interacts with the emulsion (for more information see [53]). The developing process reduces those silver bromide crystals which have interacted with radiation and contain a latent image to a black metallic silver. This metallic silver is opaque where the unexposed emulsion is transparent. The film is thereby darkened differentially to varying shades of gray based upon the amount of radiated energy that the area received. This differential darkening of the film produces the radiographic image that is examined for component status [17].

The production of the wet film radiographs used in this investigation was performed using a tube head to create the x-ray radiation, directed at an 8”x10” piece of FujiFilm IX50 Radiographic Film with two lead sheets in a sealed envelope. Samples to be imaged were placed directly upon the “film pack” and marked with lead numbers. The samples were imaged at 65 kV, 5 mA, for 2:10 minutes at a distance of 72 inches. Figure 14 shows an overview of a typical imaging setup while Figure 15 shows a standard USAF radiographic tube head.

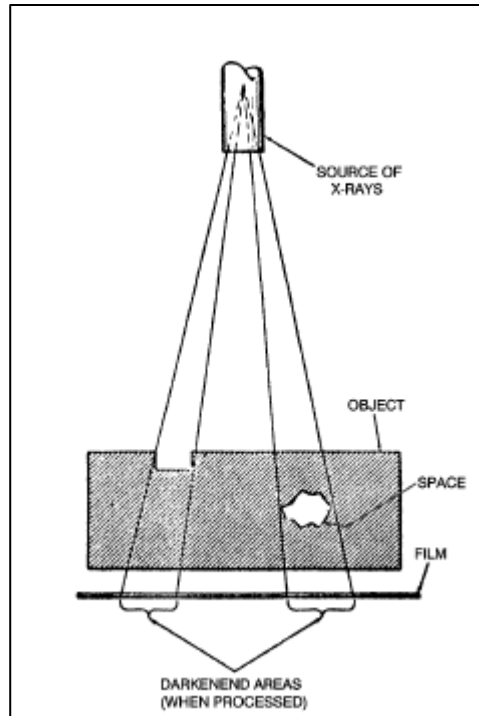


Figure 15: Diagram of radiographic exposure [17]

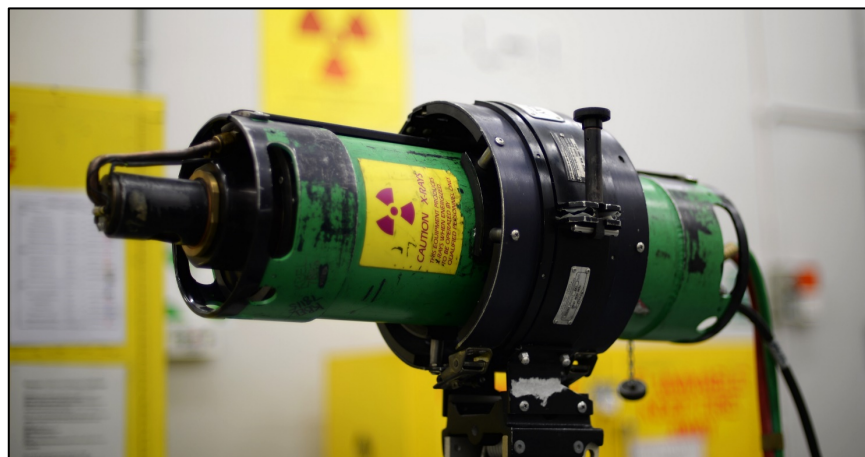


Figure 14: Standard USAF radiographic tube head [56]

To gather empirical data from wet film requires the use of a piece of equipment known as a densitometer, as shown in Figure 16. This device projects light through a piece of film using a 1mm aperture and measures the intensity of the light which is transmitted through that specific circle of film. Most densitometers return values on the film density scale, measured between 0 and

4.0. A chart showing the equations and correlations for transmittance, percent transmittance, opacity, and film density is duplicated from the Air Force NDI Technical Order 33B-1-1 [17] in Table 3.



Figure 16: X-Rite 301 Densitometer [57]

Table 3: Corresponding scales of radiographic film optical transmittance [17]

Transmittance (I_T/I_0)	Percent Transmittance (I_T/I_0) x 100	Opacity (I_0/I_T)	Film Density $\text{Log}_{10}(I_0/I_T)$
1	100	1	0
0.5	50	2	0.3
0.25	25	4	0.6
0.1	10	10	1
0.01	1	100	2
0.001	0.1	1000	3
0.0001	0.01	10000	4.0

To determine average film density of a sample on wet film a narrowly spaced interrogation grid is utilized. Measurements are taken at regular intervals and averaged to create a measurement of relative density across the sample. While measurements are dependent on the exact location in which they are taken, the film density rarely varies too much across a sample of consistent density despite the fact that the grid-like nature of the ceramic fabric is readily apparent on the radiographs. Since a minimum 2% thickness variation is the expected resolution for a radiograph, the small

variation in thickness of the fabric weaves is visible in radiographs of the CMCs used in this investigation.

4.4 Computed Tomography

Computed tomography creates a 3-dimensional model containing internal x-ray attenuation data of the interrogated specimen. This internal data is stored as a matrix of data which is presented visually using what is known as a “voxel” or a volume pixel. Each voxel represents the average CT Number (which corresponds to attenuation as discussed in Section 2.3) of the material for that given volume of the specimen. The voxel size and corresponding resolution of the CT model is determined by the equipment which is used to create the CT data.

The CT equipment used to gather the data for this investigation was a Perkin Elmer quantum FX Micro CT machine, shown in Figure 17. Samples were placed level within the imaging tube. Imaging of the samples was performed at a 30mm x 30mm field of view with a voxel representing a single 59 μm cube. The CT model covered 512 slices, each the thickness of one voxel.



Figure 17: Perkin Elmer quantum FX microCT [58]

The model can be analyzed using a variety of methods, which are divided into two main categories of bulk analysis and slice analysis. Bulk analysis uses specialized software to analyze the entire 3-D model and look for pertinent characteristics and areas of interest. Because this software was unavailable for this research effort, slice analysis was the method of choice for analysis of the CT data.

A slice is a 2-D image of a cross section, which can be taken in any of the orthogonal planes, showing data one voxel thick in the selected plane. Each slice is analyzed for its porosity using image analysis software; this investigation used ImageJ, public domain software developed by the National Institutes of Health. The software uses thresholding to find and count voxels which have a density lower than a given threshold. In thresholding, a CT number threshold is selected to isolate the pixels representing the porosity in slice. Once the pixels are isolated into categories of “porosity” and “not porosity” by this threshold, relative areas of the slice are calculated. By analyzing a large selection of slices contiguously through a specimen a quantitative analysis of the specimen’s internal characteristics can be garnered. Example images of CT slices, both pre- and post-threshold analysis are shown in Section 5.3.

4.5 Flash Thermography

Thermal Wave Imaging Inc. (TWI) provided equipment and assistance to this investigation for the gathering of the thermal imaging data. Thermographic data was gathered using a research version of the TWI commercial EchoTherm, shown in Figure 18. Samples were located within an isolating chamber and isolated from the work surface by foam insulation. The infrared camera lens and flash bulbs were located approximately 18” from the samples at the top of the isolation

chamber. The infrared camera recorded an area of 512x640 pixels, with field of view determined by camera zoom and distance.



Figure 18: Commercial EchoTherm thermographic inspection system [59]

Thermal imaging data recorded during flash thermographic investigation was provided in the form of a RAW code file. Thermal Wave Imaging Inc. provided MATLAB code and basic formatting of the RAW file structure. Translated from the RAW file, data was given as a matrix with the height and width of the detector, a depth equal to the number of frames recorded (a function of framerate and time of recording), and for each data point a 14-bit value correlating to the thermal energy recorded by the infrared camera.

Once extracted from the RAW file, this data must be processed before any meaningful analysis. The data processing is performed in the following steps:

1. A time array is created using the known framerate of the camera along with the number of frames recorded, giving a length of recording in seconds as well as the time each individual frame was recorded.
2. The frame in which the sample was exposed to the thermal flash energy is isolated by analyzing the temperature data for the maximum temperature recorded (henceforth referred to as the “Flash Frame”).
3. Using the Flash Frame, the temperature data before the thermal flash is averaged on a per pixel basis. This average is then used to normalize all of the temperature data by subtracting the corresponding pixel pre-flash average from each point of the remaining data.
4. The time array is normalized by adjusting the time array so that the Flash Frame is at zero time.

MATLAB code was written to perform these basic normalization steps immediately following the extraction of the data from the RAW file (A.A.1: AreaAnalysis.m). Using additional MATLAB code (A.A.2: RawTiffConvert.m) the normalized data matrix was used to create layered TIFF image files allowing for visual representations of the data. These representations, when examined through ImageJ or another program allowing for viewing of multiple image layers, is used to examine the change in heat radiation observed over time, as seen in Figure 19.

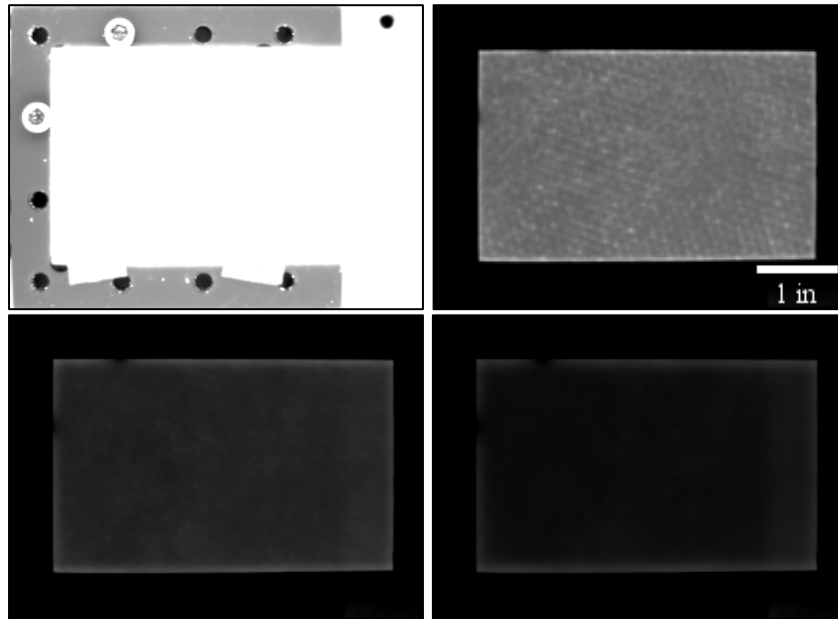


Figure 19: Stills from thermographic investigation of Set 3 sample 4. Top Left: Flash Frame (positioning bolts and table visible), Top Right: 0.5s after flash (CMC weave especially visible), Bottom Left: 1.5 s after flash, Bottom Right: 2.5s after flash. Decreasing brightness of grays indicate reduction in thermal energy at top surface.

As the visual examination and comparison of the layered TIFFs provides only qualitative information, a more quantitative analysis is required. An examination of the extracted data shows that the data has a high level of noise and artifacts. Dr. Steven Shepard of Thermal Wave Imaging Inc. describes a method known as Thermographic Signal Reconstruction (TSR):

TSR treats each pixel time history as an independent entity that is converted to a logarithmic scale to reduce dynamic range, and then fit with a low order (~8) polynomial using least squares optimization, thus creating a replica of the original data set that is free of temporal noise [45].

Another advantage of TSR is that the equation is more suitable to performing complex mathematics upon than the raw data. This includes ability to calculate smooth first and second

derivative curves of the thermographic temperature data for each pixel of the sample, which greatly reduce computational efforts.

The concept of t^* was discussed in Chapter 2, as being representative of the time when the thermal energy has diffused to the bottom surface of the sample. This was shown graphically as the time at which the slope of the temperature vs time plot (on logarithmic scales) diverged from the expected -0.5 slope. While visually simple, this computation is difficult to automate. The equation for the 2nd derivative of the temperature vs time, calculated using the TSR method, can be used to calculate t^* by taking the time of maximum value, which is much less computationally intensive (these calculations were combined with normalization steps to create: A.A.1: AreaAnalysis.m).

As each pixel has a t^* value, these values are easily assigned a grayscale value and converted to an image file (A.A.3: ThresholdImage.m). This “threshold” image, an example of which is shown in Figure 20, is used to examine relative areas of high and low diffusivity across a specimen. Quantitatively the t^* times can be averaged for areas of interest and across samples to calculate relative thermal diffusivities for those areas or samples.

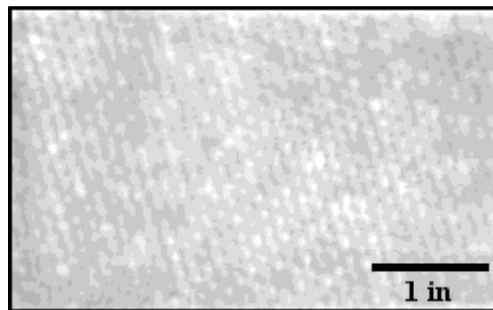


Figure 20: Threshold image of sample 5 from Set 3

Chapter 4 provided details of how data was gathered for each method used in this investigation and how that data was processed for analysis. Chapter 5 provides the processed

results from each method, analysis of the data given by each method, and examines the relationships between data sets.

Chapter 5: Results & Analysis

This chapter discusses the results of individual testing methods, examines the raw and processed data, and analyzes overall set results. Results from the individual methods are then correlated by sample and analyzed for relationships. The usefulness of these relationships toward accomplishing the research objectives is discussed in Chapter 6.

5.1 Archimedes Results

Archimedes testing was performed on the large plates (Set 1) and the porosity coupon set (Set 3). Archimedes testing could not be performed with any accuracy on the representative aircraft components (Set 2) due to the geometry of the components and inclusion of metallic components within the assemblies. The results of the Archimedes testing are shown in Table 4 and Table 5 for Sets 1 and 3, respectively. This data is reported in percentage porosity within the samples.

Table 4: Archimedes porosities of Set 1

Plate	Porosity [%]
1461	22
1450	8

Table 5: Archimedes porosities of Set 3

Sample	Porosity [%]
2	20.15
3	15.02
4	10.66
5	8.19
6	6.3
7	5.44
8	3.49
9	3.2
10	1.92
11	1.31

5.2 Radiographic Results

Radiographic testing was performed on the Set 3 coupons. Figure 21 shows two radiographs of the Set 3 coupons on a film viewer. Eight of ten samples from Set 3 were imaged in each radiograph (though only six are visible in Figure 21); samples which were imaged on both radiographs were used to confirm that the imaging remained controlled from radiograph to radiograph. The samples were marked in the radiographs by placing lead numbers on the samples which attenuate much more radiation and create the lighter area (blue arrows).

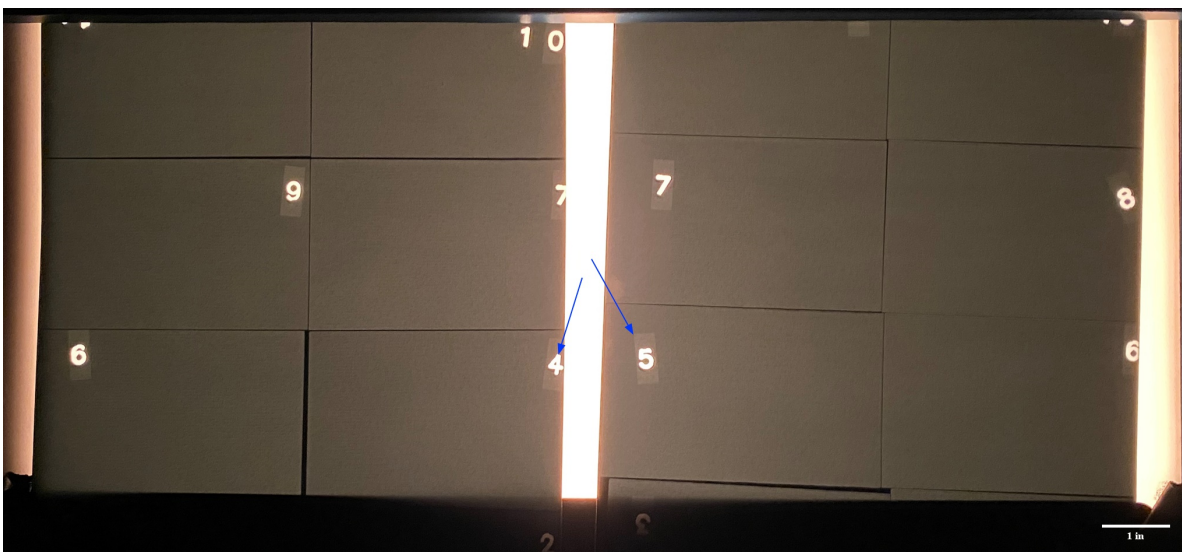


Figure 21: Two radiographs of Set 3 on a film viewer.

Using the densitometer, each sample was examined for its relative film density in an evenly spaced 5 by 5 grid. The interrogation grid from sample 4 is shown in Table 6.

Table 6: Interrogation grid data taken from sample 4 of Set 3

Sample:		4			Avg:	2.508
2.49	2.5	2.52	2.52	2.54		
2.46	2.49	2.51	2.52	2.53		
2.48	2.49	2.51	2.51	2.51		
2.48	2.51	2.52	2.54	2.46		
2.5	2.51	2.54	2.57	2.48		

The results of the interrogation grids for each coupon were averaged to give a representative film density for each sample as shown in Table 7.

Table 7: Average film density for all samples of Set 3

Sample	Film Dens.
2	2.591
3	2.534
4	2.508
5	2.503
6	2.506
7	2.473
8	2.468
9	2.410
10	2.400
11	2.384

5.3 Computed Tomography Results

Computed tomography testing was performed on two of the Set 3 coupons, samples 4 and 7, with Archimedes calculated porosities of 10.7% and 5.4% respectively. Testing was limited due to several factors including the availability of equipment and the accessibility of analysis resources. To perform slice analysis of the CT data, each data set was converted to 512 grayscale

slices covering the entirety of the interrogation area. A single slice from sample 7, which has been cropped for analysis, is shown in Figure 22.



Figure 22: Slice from sample 7 CT data, porosity visible throughout slice

To perform slice analysis, a threshold is selected which accurately isolates the areas in the scan that are representative of porosity. The image is converted to binary, as shown in Figure 23 for the same slice of sample 7 pictured in Figure 22; areas in black are areas which fell below the set threshold density indicating they are an area of porosity.

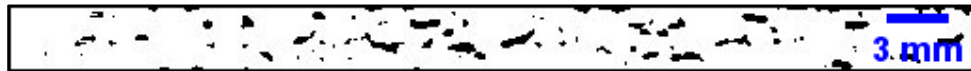


Figure 23: Slice from Figure 15 converted to binary, black areas represent porosity

ImageJ automatically calculates the percentage by area in each slice image that is below this threshold. By analyzing each slice taken from a sample, the total internal porosity of that sample can be characterized with exceptional accuracy and the data used to corroborate other methodology results, as discussed in section 5.5. The average sample porosity for the imaged areas of the two samples is shown in Table 8.

Table 8: CT porosity data for samples 4 & 7 from Set 3

Sample	Porosity [%]
4	10.55
7	5.54

5.4 Flash Thermography Results

Flash thermographic testing was performed on all three sets of CMC samples. Example images from Set 3 and the Set 1 Sample Plates are shown below. Due to the proprietary nature of the Set 2 representative aircraft components, only narrow images will be presented.

Several threshold images from the aircraft components are shown below. As discussed in Section 4.5, threshold images are a graphical representation of the t^* values for each interrogation. While the aircraft components do not provide extensive quantitative data to be correlated with other data sets, they qualitatively demonstrate several important characteristics of thermographic inspection.

Figure 24 demonstrates the importance of knowing the thickness of the sample which is being investigated. The changing thicknesses of the aircraft component is readily apparent across Figure 24 in the changing of the t^* values. Note, colors in Figure 24 through Figure 27 will appear inverted to those in Figure 10 due to difference in threshold and temperature over time images.



Figure 24: Thermographic threshold image of Set 2 sample, two different thickness of sample are visible, thicker (top), thinner (bottom)

Figure 25 shows an area where two metal components are bonded to the back surface of the aircraft component CMC. The depicted area is of the same thickness of CMC material (apart from the edges of the component at the top corners), however the back surface of the component

is exposed to the varying thermal diffusivities of metal and air, creating the difference in t^* values visible.

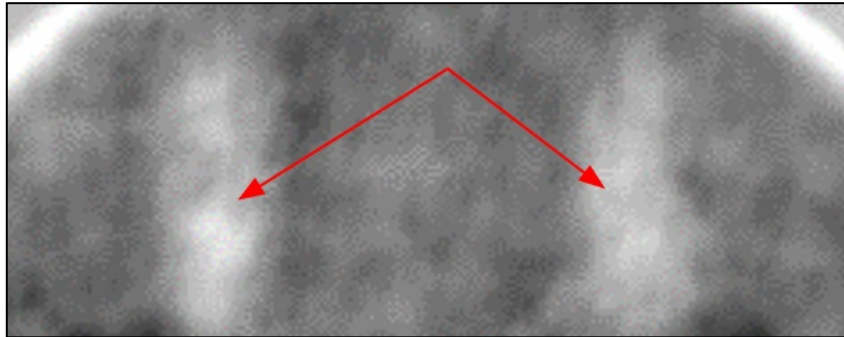


Figure 25: Thermographic threshold image of Set 2 sample, two areas (red arrows) where metal components are bonded to back surface

Figure 26 depicts an area at an edge of the component where there is no change in geometry or material thickness, nor is the material composition significantly different at the edge. It is visually apparent that along the edge of the component there is an area of consistently differing t^* value. This behavior is due to the “wraparound” of the thermal wave and is an artifact of the thermographic inspection process. This “edge effect” on the inspection of the component creates an area that provides substantial difficulty in inspecting effectively, and as such is excluded from analytical results in common practice [14].

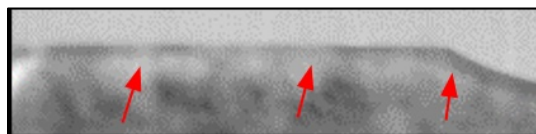


Figure 26: Thermographic threshold image of Set 2 sample, area at edge of component, “edge effect” (red arrow) visible along length of edge

Figure 27 shows an area where a circular metal insert has been formed into the component, through the CMC material. Around this insert a similar “edge effect” can be seen as described above. However as opposed to being exposed to comparatively insulating air, this interior edge is

in contact with a material with a substantially higher conductivity. The conduction by this metal insert of heat through the composite substantially affects the apparent t^* values of the CMC surrounding it. This image also shows a large area in which the CMC material has an inter-layer disbond. This is apparent in the large area which is represented as nearly black, indicating that the heat took a comparatively long time to propagate through this area due to the disbond interruption of the material.

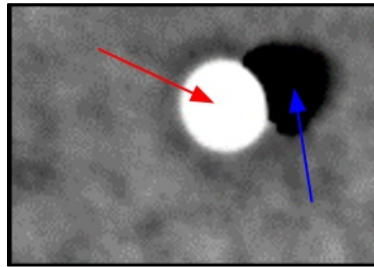


Figure 27: Thermographic threshold image of Set 2 Sample, metal inset (red arrow) with disbond (blue arrow)

The thermographic results from the investigation of Set 3 provide substantially more quantitative data. Using threshold images, a region of interest was selected for each sample that excluded the areas where the “edge effect” would prevent accurate data collection. The t^* value for each sample in the region of interest was calculated and is shown in Table 9.

Table 9: Thermographic t^* data averages for Set 3

Sample	t^* [sec]
2	6.76
3	6.15
4	4.87
5	4.15
6	3.52
7	3.18
8	2.95
9	2.88
10	2.81
11	2.67

5.5 Analysis

The Archimedes data for Set 3 reveals the range of porosities across the samples and is used as a baseline for the radiographic, tomographic, and thermographic testing results. While the Archimedes testing provides some of the most reliable data regarding porosity within the samples, this method of testing could not be used on a component either in-situ or when integrated into a larger assembly. By correlating the results of the other testing methods with this porosity data, this investigation examined the possibility of using results of radiographic, tomographic, or thermographic testing to calculate porosity. Table 10 compiles the data for Archimedes, thermographic, and radiographic testing of Set 3. Table 11 integrates the Computed Tomography data for those samples on which CT was performed and the percent difference to Archimedes results.

Table 10: Archimedes porosity, thermographic t*, and radiographic film density results for Set 3

Sample	Archimedes Porosity [%]	t* [sec]	Film Dens.
2	20.15	6.76	2.591
3	15.02	6.15	2.534
4	10.66	4.87	2.508
5	8.19	4.15	2.503
6	6.3	3.52	2.506
7	5.44	3.18	2.473
8	3.49	2.95	2.468
9	3.2	2.88	2.410
10	1.92	2.81	2.400
11	1.31	2.67	2.384

Table 11: Archimedes and CT porosity, thermographic t*, and radiographic film density for samples 4 & 7 of Set 3

Sample	Archimedes Porosity [%]	t* [sec]	Film Dens.	CT Porosity [%]	% Diff.
4	10.66	4.87	2.508	10.55	1.03
7	5.44	3.18	2.473	5.54	1.84

Due to the high accuracy of CT investigation when looking at an individual slice for specific data, that data can be treated as accurate as destructive microscopy for the purposes of this investigation. The results from automated threshold analysis showed values that varied less than 2% from those given by Archimedes testing (shown in final column of Table 11). This close concurrence of Archimedes and Computed Tomography porosity results indicates that the Archimedes data can be treated as reliable for correlative usage and used as an accurate baseline.

Graphing the thermographic and radiographic results versus the results from Archimedes testing provides a clear view of how the results of those methods correlate with the porosity of the sample. The results of the radiographic testing are presented in Figure 28. A linear trendline was plotted against the data but provided limited correlation with an R-squared value of 0.848. This is a statistically non-trivial correlation; however, for use as a tool for determining sample porosity this model would provide substantial accuracy concerns.

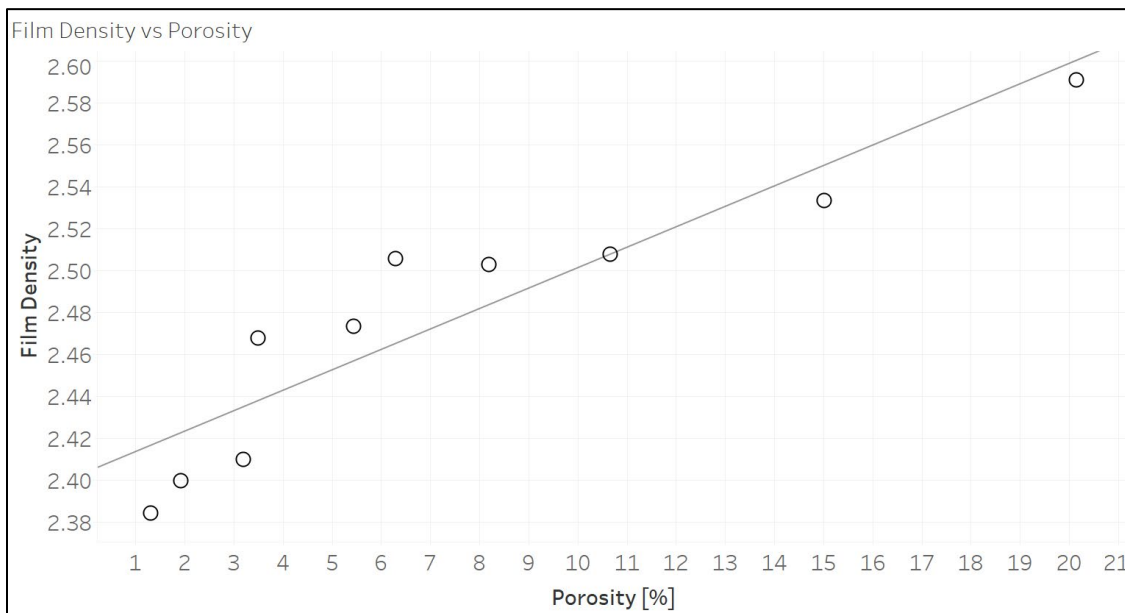


Figure 28: Set 3 radiographic film density vs porosity, linear trendline

Fitting a third order polynomial trendline to the data, as shown in Figure 29, provided a more statistically significant model for this data. The polynomial trendline has an R-squared of 0.955 and as the higher R-squared value indicates, the polynomial trend fits the data much more accurately and would seem to serve as a better predictor of porosity for given film density. While this would seem to serve as an accurate model, higher order polynomials may indicate greater correlation than actually exists, and there is no readily apparent physical causality to indicate the accuracy of a 3rd order function beyond high correlation.

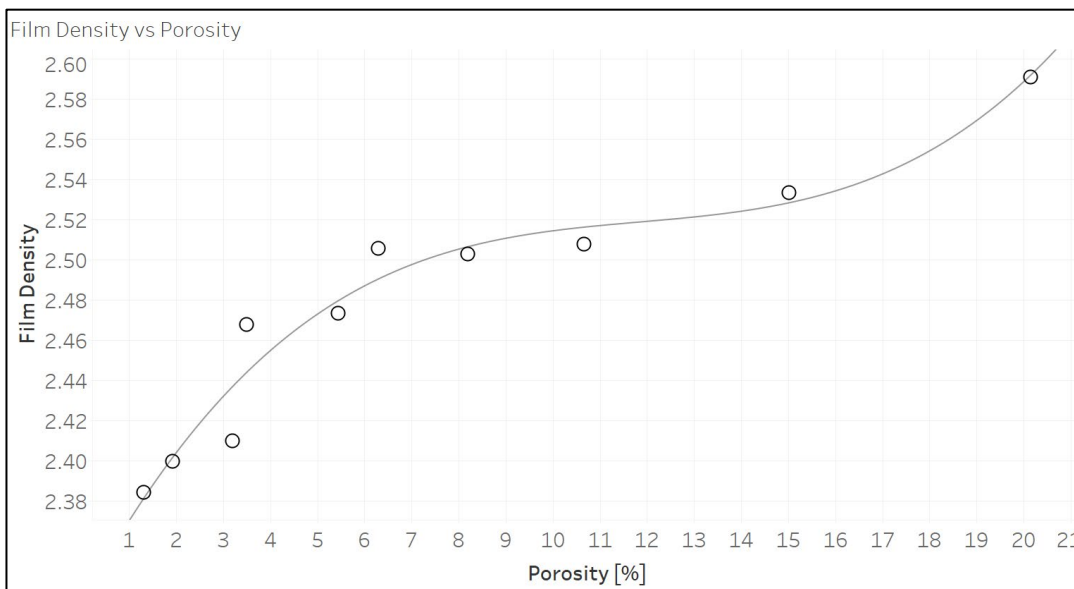


Figure 29: Set 3 radiographic film density vs porosity, 3rd order polynomial trendline

Industrial X-ray film is expected to darken on a log scale proportional to the amount of exposure that is received [54]. The characteristic curve chart for Fuji Industrial X-ray Film is shown in Figure 30. Fuji IX50 film was used in this investigation, though it should be noted that this graph is not capable of predicting film density vs exposure of the Set 3 samples, as the chart is generated for a specific radiographic exposure not indicative of that used by this investigation.

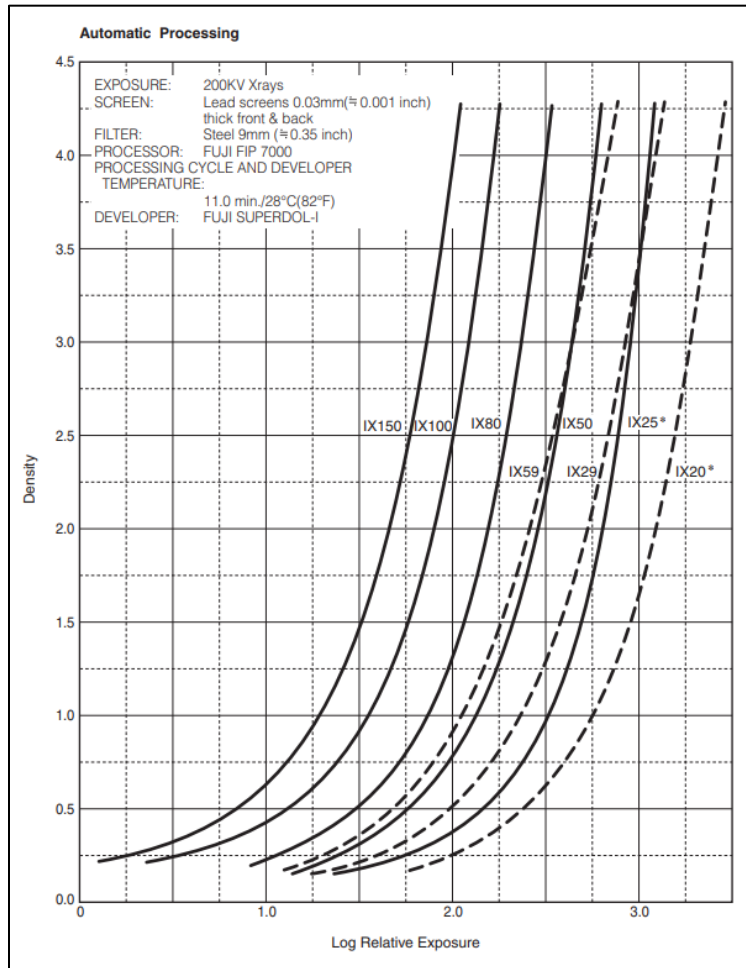


Figure 30: Fuji radiographic films characteristic curves [54]

Figure 30 does indicate that fitting a logarithmic trendline would provide a meaningful correlation model. Figure 31 is the same film density vs porosity data with a logarithmic trendline fitted. The logarithmic trendline has an R-squared value on 0.927, which is about 3% less than the correlation for the polynomial trendline. While both logarithmic and polynomial models result in high correlations to the presented radiographic data, there is no definitive substance to using either as a model for analytically determining porosity using radiographic results.

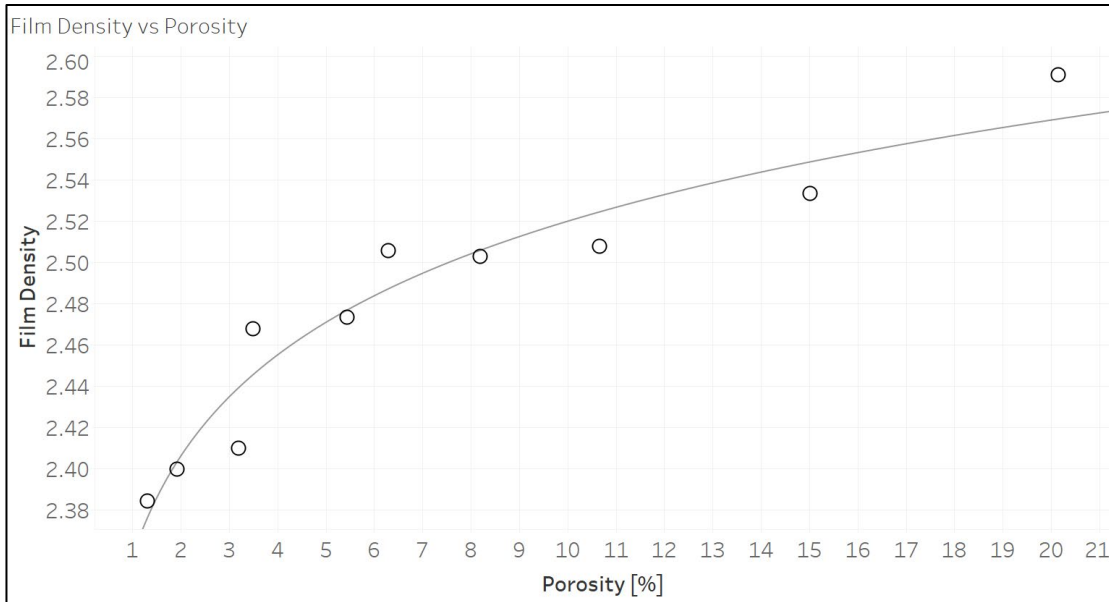


Figure 31: Set 3 radiographic film density vs porosity, logarithmic trendline

The results of the thermographic testing on Set 3 are shown in the Figure 32, plotted against the sample Archimedes calculated porosity. The linear trendline has an excellent R-squared correlation value of 0.979, displaying none of the issues with trending that radiographic testing displayed.

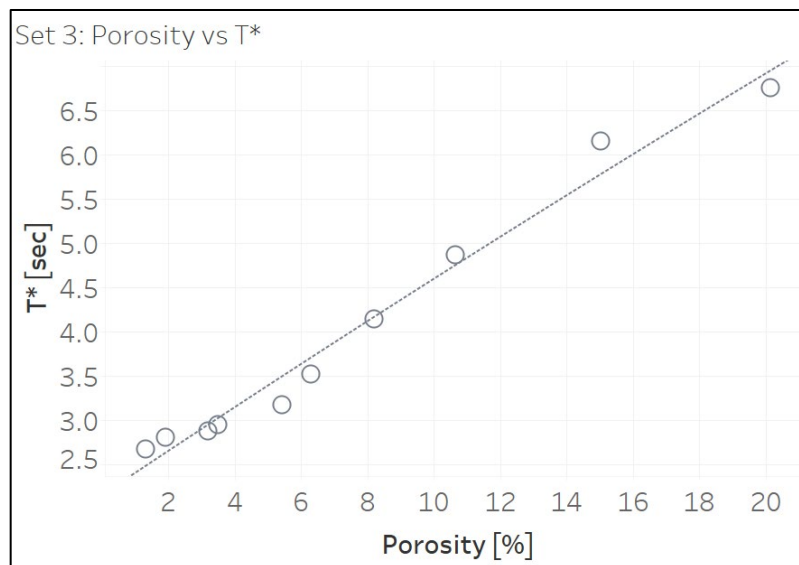


Figure 32: Set 3 thermographic t* vs porosity

The linear trendline provides an equation that can be used with relatively high accuracy to determine the sample porosity. This approach is limited to samples of the same material and thickness which substantially limits the usefulness. By rearranging Equation 14 the results for t^* can be converted to the material thermal diffusivity value, α .

Table 12: Set 3 Archimedes porosity, thickness, thermographic t^* , & calculated α

Sample	Porosity [%]	Tavg [cm]	t^* [sec]	α [cm ² /s]
2	20.15	0.2720	6.758	0.00348
3	15.02	0.2705	6.154	0.00378
4	10.66	0.2695	4.869	0.00475
5	8.19	0.2711	4.148	0.00564
6	6.3	0.2758	3.521	0.00688
7	5.44	0.2756	3.176	0.00761
8	3.49	0.2707	2.949	0.00791
9	3.2	0.2705	2.878	0.00809
10	1.92	0.2690	2.808	0.00821
11	1.31	0.2705	2.674	0.00871

Table 12 shows the calculated thermal diffusivity for Set 3, along with the calculation values of t^* and sample thickness. The results of α vs porosity are shown in Figure 33. The correlation for the trendline is still quite significant with an R-squared value of 0.930, though the uncertainty has increased with the additional measurements of the thickness.

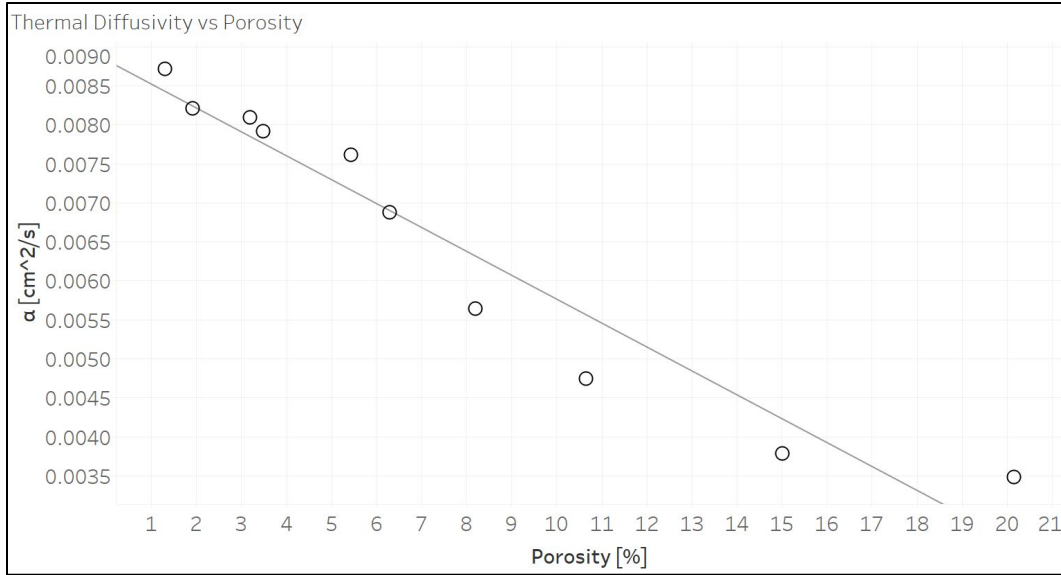


Figure 33: Set 3 thermal diffusivity vs porosity

The trendline equation gives a theoretical method for turning results of thermographic investigation into a calculated porosity. The equation from the trendline gives:

$$Porosity = -3035.72 * \alpha + 27.3208 \quad [16]$$

Equation 14 can be rearranged and substituted into Equation 16 for α resulting in:

$$Porosity = -3035.72 * \frac{T^2}{\pi * t^*} + 27.3208 \quad [17]$$

The combined Equation 17 provides a manner for determining the porosity from a panel of known thickness of S200 CMC. The accuracy of this equation can be confirmed by using the results of the investigations from the large plate samples of Set 1. Table 13 presents the data in Table 12 for the Set 1 samples.

Table 13: Set 1 Archimedes porosity, thickness, thermographic t^* , & calculated α

Sample	Archimedes Porosity [%]	T [cm]	t^* [sec]	α [cm ² /s]
1461	22	0.5133	24.34	0.00344
1450	8	0.5108	12.785	0.00650

Simply taking the t^* value of the Set 1 results and plotting them on Figure 33 with the Set 3 data would not provide the correct porosities of the Set 1 samples. By utilizing Equation 17, as derived from the Set 3 data, the differing thickness of the Set 1 samples is accounted for, resulting in the calculated porosities shown in Table 14.

Table 14: Set 1 Archimedes porosity & thermographically calculated porosity

Sample No	Archimedes Porosity [%]	Calculated Porosity [%]	% Difference
1461	22	16.86	23.4
1450	8	7.60	5.0

The calculated porosities are of mixed accuracy, with differences to the Archimedes results of 5.0 % and 23.4%. As Archimedes results are only reported to the single digits, this error is only approximate. Additionally, as shown in Figure 34, Sample 1461, which has the higher disparity, displays a large variation in t^* across the sample. The variation does not mathematically account for the error, however it does indicate that the sample may not display the expected properties.

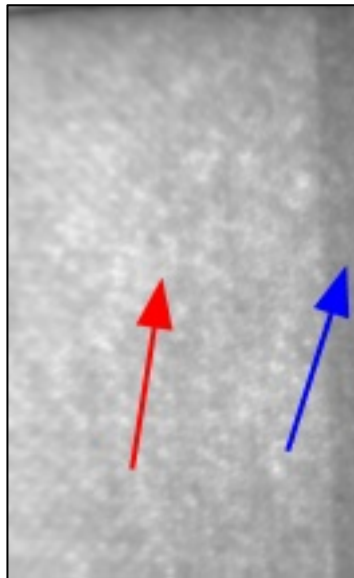


Figure 34: Threshold image of sample 1461 with areas of varying t^* visible, (higher value – red arrow, lower value – blue arrow)

As the Set 2 samples were only exposed to thermographic testing, there are no porosity measurements which can be used for comparison. However, the thermographic testing still gathered quantitative data that can be analyzed for items of interest. Table 15 shows data from Set 2 samples of thermographic results, calculated thermal diffusivity, and percent porosity. The porosity value is calculated using Equation 17 derived from Set 3 thermal diffusivity and porosity values. Two samples are represented in Table 15. Sample 1 has data taken from one area. Sample 2 has data taken from two areas, where the areas are of different thicknesses.

Table 15: Set 2 Thermographic t^* , calculated thermal diffusivity and porosity

Sample	t^* [sec]	α [cm ² /s]	Porosity [%]
1 (Air)	14.450	0.00527	11.39
2 (Thin)	4.956	0.00457	13.51
2 (Thick)	16.080	0.00473	13.01

The data shows a narrow range of porosities, of about 11.4-13.5%. This is a believable range for components that have been in service, though without other testing these numbers are unconfirmed. Sample 2 shows extremely similar porosity values across the sample, though due to the change in thickness, the t^* values are quite disparate. This confirms that the method is viable for components of more complex geometry if the thickness in the area is known.

Chapter 5 presented the results of each testing method and then discussed how those results correlated. Models were discussed for their ability to predict sample porosity and applied to varying sample sets to examine accuracy and usefulness. Chapter 6 provides the conclusions drawn from this investigation and discusses future work building upon the results and efforts heretofore discussed.

Chapter 6: Conclusions & Future Work

Chapter 6 discusses the conclusions that can be drawn from the efforts of this investigation, with a particular focus on answering the research objectives discussed in Section 1.7. The objectives of this investigation were to examine the CMC inspection capabilities and limitations of the various NDT methods available to this investigation, and to compare the results of those available NDT methods for their abilities, relative accuracies, and ease of use in determining porosity in both relative and absolute analysis of CMCs, including the ability to quantitatively determine porosity in a sample using derived equations from thermographic inspection results.

6.1 Conclusions

The NDT methods available to this investigation were Archimedes (as performed by the CMC sample manufacturers), traditional film radiography, computed tomography, and flash thermography. Each method presented its own set of capabilities and limitations when performing an interrogation of the CMCs and presented varying degrees of success in determination of porosity within the samples.

6.1.1 Archimedes Testing

Archimedes testing is capable of determining the density, and corresponding sample porosity, with a high level of accuracy and with limited specialized equipment or skill required, and no need of a reference standard for comparison. The accuracy of the analysis is limited by the accuracy of the volume measurement of the sample. The fluid used (which must be carefully chosen as CMCs are extremely moisture absorbent) can have direct effects on the volume measurement as surface tension of the fluid and absorption by the component will determine the

effects of surface energy and porosity on the volume measurement. Samples which contain foreign objects (such as the representative aircraft components of Set 2) cannot be analyzed using Archimedes unless the analysis is performed prior to those foreign objects being integrated. Furthermore, any sample to be analyzed cannot have been integrated into a higher assembly and must fit within the volume measurement vessel.

Archimedes testing, while being much less intensive in terms of testing and data analysis, provided data that was validated as accurate through correlation with Computed Tomography. The Archimedes porosity and density data was used as the primary reference standard for all other methods used by this investigation.

6.1.2 Film Radiography Testing

Film radiography can provide clear imaging of the overall and internal state of a sample as viewed in one direction, by recording the relative radiation attenuation of the imaged object. The equipment used to interrogate samples and record the data is highly specialized and can be quite dangerous without the proper user training. Data gathering must also be highly controlled, as each shot must maintain the same parameters for the results to be consistent across interrogations of the same sample or for dissimilar samples to give results on the same scale. Access to both sides of a sample is required, and the method yields best results on flat surfaces where the sample is equidistant to the radiation source across its entirety.

The film density data provided by film Radiographic Testing was manually analyzed using a densitometer and an evenly spaced interrogation grid which was averaged to give a quantitative measurement for each interrogated sample. While this measurement is not tremendously intensive, the precision is dependent upon the grid spacing and number of interrogation points. The use of

digital or computed radiography would have allowed for simpler and more accurate analysis using software to determine average “film” density across the area of interest.

As there is no simple way to know the precise amount of radiation impinged upon the sample or what is transmitted through to the film, it is not possible to make an absolute measurement of the radiation attenuation of the samples. Without this data, it is very difficult to make an accurate assessment of porosity effect on radiographic attenuation. The relatively small differences in film density and concerns about using the correct model indicate that this is not a reliable method for determining sample porosity. Without further work, radiography can only accurately determine porosity by using a reference standard created with the same shots used for data collection.

6.1.3 Computed Tomography Testing

Computed tomography uses many of the same basic principles and physics as radiography, however the digital nature and full rotational examination provide much more extensive data. The data provided by CT gives a clear internal view of the component with each volume pixel representing the CT Number of that area in space. If the varying CT numbers can be correlated to variations in the physical makeup of the component, then the CT data provides an exact representation of the object dependent on the resolution of the scanner. The gathering of this data can be extremely time intensive based upon the required resolution, size of the object being imaged, and relative radiation attenuation of the object. Additionally, the data analysis can be time and resource intensive based upon method of analysis and size of the imaged area. Furthermore, the sample being imaged must fit entirely within the CT equipment (the equipment used by this investigation was only capable of fitting the smallest samples, those of Set 3).

The nature of the data provides such great insight into the samples that it is nearly the equal of destructive microscopy for determining the interior make up of a sample. As the samples used by this investigation were not permitted to be destroyed, CT is only manner for reliably determining true porosity of the samples and validating the accuracy of the Archimedes-derived porosity data. The uncertainty created by using automated threshold analysis is minimal and the results of the CT porosity analysis is an absolute measurement with no need for a reference standard.

6.1.4 Flash Thermography Testing

Flash thermography provides data representative of the way that thermal energy moves through a sample by imaging the behavior of heat energy emitted by the top surface of the sample. The data collection itself is quite efficient in terms of time and effort, however, anything which affects the transport of that heat energy, be it sample structure, porosity, inclusions, water absorption, back surface condition, or other defect, is visible when performing the analysis. While this is useful if investigating only in a qualitative manner (examining the object for areas where something is different), if attempting to perform absolute analysis of sample porosity each of those factors and more must be controlled or understood.

The data gathered by this investigation using flash thermography was intensively processed to give useable information, though once the analysis code was written, the computational effort was minimal. The analysis of all three sample sets gave insight into the abilities of Thermography to determine porosity in those samples. The analysis of Set 3 created the equation used to determine porosity across the other samples. Set 1 was used to validate the viability of the equation for use on samples investigated in the same methodology and of the same material but of a different

thickness and gave mixed results. If sample 1461, which displayed irregular values across the sample, is excluded, this did show that once the equation had been determined, a true reference standard was not necessary to calculate porosity. The calculations can be quite sensitive to small changes in measured t^* , however the relatively high accuracies of calculations using the TSR method minimize the effect of this sensitivity. Set 2 components showed how the determined equation could again be used reliably on samples of different thickness and geometries, but that a metal object bonded to the back surface makes that area unable to be analyzed effectively.

6.1.5 Summary

Internal porosity is one of the driving factors in reduced strength and fatigue properties of CMC-based components. Four methods were used by this investigation to examine S200 CMC samples for sample porosity. Archimedes can determine sample density and corresponding porosity levels with high accuracy but requires the entire component to be immersed within a fluid, which creates corresponding risks of moisture absorption by the CMC. Computed Tomography allows for high resolution internal imaging of the components and was used to corroborate the results of Archimedes testing. While CT provides the best look at the internal state of a component short of microscopy (which could not be accomplished on the samples available to this investigation) CT also requires components to fit entirely within the imaging equipment and is extremely data and analysis intensive. Radiographic testing is much simpler from a data analysis standpoint, and while it still requires access to the back surface of the component, does not require that the component fit within a limiting piece of equipment. However radiographic inspection provided limited insight to the amount of porosity within a sample and would require a reference standard of equivalent size and thickness to determine porosity of any component inspection.

Thermographic inspection requires access to only one side of the component under investigation (though knowledge of the back surface condition is required to provide accurate data, and certain conditions will make it difficult or impossible to accurately inspect) and requires limited data analysis effort once programmed. The data gathered by flash thermography is highly correlative to sample porosity, and an equation for determining component porosity using thermographic data and known sample thickness was derived and validated with promising results. Future work, as discussed in Section 6.2, must be performed to determine the effects of additional factors on inspections, examine alternative methods of investigation, and confirm the results of this investigation using additional testing and mathematical modeling.

6.2 Future Work

Additional work is required to improve the reliability of Thermographic Testing for porosity determination. This work is centered around cataloging, understanding, and controlling the effect of variables on the thermographic results. This also includes validating the equation derived by this investigation and the results of Set 1 thermographic testing. Some of the factors to be investigated include edge effects around external edges, insulated edges, and edges exposed to a higher conductivity material, the effects of varying porosity shapes and material weave orientations, and the potential effects of moisture absorption on thermal diffusivity. Differences in thermal energy imparted to the sample should be examined to ensure testing reliability. Varying back surface conditions should be analyzed to determine methodology for examining components which are integrated into larger structures. Materials with larger and smaller thermal diffusivities should be examined to determine the viability of an equation which can take base material thermal conductivity as an input and calculate material porosity without need of using a reference set to

create an equation. Mathematical calculations and finite element analysis should be performed to determine if the empirical results correlate with theoretical modeling or if there are additional factors which interfered with accurate results of this study. Destructive microscopy should be performed to determine the accuracy of Archimedes and Computed Tomography porosity results.

Future work should also consist of a broader spectrum of Non-Destructive Inspection methods to determine if any offer advantages or disadvantages not seen with the utilized methods. Air-coupled ultrasonics are of particular interest as they are unlikely to be affected by back surface conditions as much as thermographic inspections, while not damaging the CMCs through moisture absorption. Other thermographic inspection techniques should be examined, such as through-thickness, to determine if they offer an advantage over flash thermography. All work should be performed on other CMC materials to determine if cross-material correlations exist and if the advantages and limitations of each method are consistent.

References

- [1] The American Society for Nondestructive Testing, "Introduction To Nondestructive Testing," [Online]. Available: https://www.asnt.org/MajorSiteSections/About/Introduction_to_Nondestructive_Testing.aspx.
- [2] C. Altan, *Composite Materials Lecture Slides*, Norman, 2018.
- [3] M. Futterman, "Nike Vaporfly Shoes Avoid Olympics Ban," *The New York Times*, 2020.
- [4] R. Minder, "Portugal Is Riding a Boom in Bicycles," *The New York Times*, Vouzela, 2021.
- [5] W. Krenkel, *Ceramic Matrix Composites: Fiber Reinforced Ceramics and Their Applications* / Edited by Walter Krenkel, 2008..
- [6] S. G. Zhu, H. X. Qu and C. X. Ouyang, "Hot pressing of tungsten carbide ceramic matrix composites," in *Advances in Ceramic Matrix Composites, Second Edition, Edited by I. M. Low*, 2018.
- [7] T. Behrendt, S. Hackemann, P. Mechnich, Y. Shi, S. Honig, S. Hofmann and D. Koch, "Development and Test of Oxide/Oxide Ceramic Matrix Composites Combuster Liner Demonstrators for Aero-engines," *Journal of Engineering for Gas Turbines and Power*, vol. 139, 2017.
- [8] K. K. Chawla, *Composite Materials Science and Engineering Third Edition*, New York: Springer, 2012.
- [9] COI Ceramics, Inc., "Nicalon Ceramic Fiber," 17 January 2006. [Online]. Available: <http://www.coiceramics.com/pdfs/Nicalon.pdf>. [Accessed 8 December 2020].
- [10] D. Balageas, X. Maldague, D. Burleigh, V. P. Vavilov, B. Oswald-Tranta, J.-M. Roche, C. Pradere and G. M. Carlomagno, "Thermal (IR) and Other NDT Techniques for Improved Material Inspection," *Journal of Nondestructive Evaluation*, vol. 35, pp. 1-17, 2016.
- [11] W. A. Ellingson, C. M. Deemer, J. Sun and E. R. Koehl, "NDE Technology for Ceramic Composites," in *Proceedings of GT2006*, Barcelona, 2006.
- [12] J. G. Sun, M. J. Verrilli, R. R. Stephan, R. T. Barnett and G. C. Ojard, "Nondestructive Evaluation of Ceramic Matrix Composite Combuster Components," in *29th Annual*

Review of Progress in Quantitative Nondestructive Evaluation Programs, Bellingham, 2003.

- [13] H. Mei, Y. Xu, L. Cheng and L. Zhang, "Nondestructive Evaluation and Mechanical Characterization of a Defect-Embedded Ceramic Matrix Composite Laminate," *International Journal of Applied Ceramic Technologies*, vol. 4, pp. 378-386, 2007.
- [14] U. Santhosh, Y. Gowayed, G. Ojard, I. Smyth, S. Kalarikkal and G. Jefferson, "Quantification of Porosity in Ceramic Matrix Composites Using Thermography," *Journal of Nondestructive Evaluation*, vol. 37, 2018.
- [15] P. J. Meltzer, "Ceramic Matrix Composite seals proving reliable for jet engine nozzles," 8 July 2008. [Online]. Available: <https://www.wpafb.af.mil/News/Article-Display/Article/400832/ceramic-matrix-composite-seals-proving-reliable-for-jet-engine-nozzles/>.
- [16] U.S. Small Business Administration, "Design and Life Prediction Methodologies for Weight Efficient Ceramic Matrix Composite (CMC) Propulsion Components," 2004. [Online]. Available: <https://www.sbir.gov/sbirsearch/detail/225797>. [Accessed 1 November 2020].
- [17] United States Air Force, "TO 33B-1-1 Nondestructive Inspection Methods, Basic Theory," 15 October 2016. [Online]. Available: <https://www.tinker.af.mil/Portals/106/Documents/Technical%20Orders/AFD-101516-33B-1-1.pdf>.
- [18] E. A. Lindgren, J. Brausch, C. Buynak and C. Babish, "Recent and Future Enhancements in NDI for Aircraft Structures (Postprint)," November 2015. [Online]. Available: <https://apps.dtic.mil/sti/pdfs/AD1002280.pdf>.
- [19] National Transportation Safety Board, "Aircraft Accident Report Aloha Airlines, Flight 243," 14 June 1989. [Online]. Available: <https://www.ntsb.gov/investigations/AccidentReports/Reports/AAR8903.pdf>.
- [20] F. Bashir, "The Unfateful Aloha Airlines Flight 243," *Aviation Geeks*, 22 April 2021. [Online]. Available: <https://aviationgeeks1.com/the-unfateful-aloha-airlines-flight-243/>.
- [21] National Transportation Safety Board, "Aircraft Accident Report, United Airlines Flight 232," 1 November 1990. [Online]. Available: <https://www.ntsb.gov/investigations/AccidentReports/Reports/AAR-90-06.pdf>.
- [22] D. Chapel and D. Kemme, "Comparisons and Lessons Learned from UA232 Sioux City and AA383 Chicago Uncontained Events," [Online]. Available: <https://www.isasi.org/Documents/Awards/Comparisons%20and%20Lessons%20Learned>

%20from%20UA232%20Sioux%20City%20and%20AA383%20Chicago%20Uncontained%20Events.pdf. [Accessed 10 October 2021].

- [23] National Transportation Safety Board, "Powerplants Group Chairman's Factual Report," 13 February 2018. [Online]. Available: <https://data.ntsb.gov/Docket?ProjectID=96738>.
- [24] H. Berger and D. o. T. I. U.S. Atomic Energy Commission, *Nondestructive Testing*, Oak Ridge: U.S. Atomic Energy Commission, Division of Technical Information, 1969.
- [25] Iowa State University Center for Nondestructive Evaluation, "History of Penetrant Inspection," Iowa State University, [Online]. Available: <http://www.ndt-ed.org/EducationResources/CommunityCollege/PenetrantTest/Introduction/history.html>. [Accessed 8 November 2020].
- [26] I. S. U. C. f. N. Evaluation, "Reference Standards," Iowa State University, [Online]. Available: <https://www.ndt-ed.org/NDETTechniques/EddyCurrent/Procedures/ReferenceStandards.xhtml>. [Accessed 10 October 2021].
- [27] W. C. Rontgen, "On a New Kind of Rays," *Science*, vol. 3, no. 59, pp. 227-231, 1896.
- [28] Lumen Learning, "The Electromagnetic Spectrum," Lumen Learning, 11 November 2020. [Online]. Available: <https://courses.lumenlearning.com/boundless-physics/chapter/the-electromagnetic-spectrum/>.
- [29] J. T. Bushberg, J. A. Seibert, E. M. Leidholdt Jr and J. M. Boone, *The Essential Physics of Medical Imaging Third Edition*, Philadelphia: Lippincott Williams and Wilkins, 2012.
- [30] S. M. Midgley, "A parameterization scheme for the x-ray linear attenuation coefficient and energy absorption coefficient," *Physics in Medicine and Biology*, vol. 49, pp. 307-325, 2004.
- [31] H. Liu, *Medical Imaging Systems Class Notes*, Norman, 2018.
- [32] N. Fabris and R. Lopez, *Materials and Processes for NDT Technology Second Edition*, Columbus: The American Society for Nondestructive Testing, Inc., 2016.
- [33] D. A. Kaminski and M. K. Jensen, *Introduction to Thermal and Fluids Engineering*, Hoboken: John Wiley & Sons, 2005.
- [34] Iowa State University Center for Nondestructive Evaluation, "Scientific Principles of Thermal Testing," Iowa State University, [Online]. Available: https://www.ndt-ed.org/NDETTechniques/Thermography/IR_Science.xhtml. [Accessed 10 October 2021].

- [35] Y. A. Cengel and A. J. Ghajar, *Heat and Mass Transfer Fundamentals & Applications Fifth Edition*, New York: McGraw-Hill Education, 2015.
- [36] Y. A. Cengel and A. M. Boles, *Thermodynamics An Engineering Approach Seventh Edition*, New York: McGraw-Hill, 2011.
- [37] J.-C. Han, *Analytical Heat Transfer*, Boca Raton: Taylor & Francis Group, 2012.
- [38] R. B. Bird, W. E. Stewart and E. N. Lightfoot, *Transport Phenomena Revised Second Edition*, New York: John Wiley & Sons, 2007.
- [39] C. Christov, "On frame indifferent formulation of the Maxwell-Cattaneo model of finite-speed heat conduction," *Mechanics Research Communications*, vol. 36, pp. 481-486, 2009.
- [40] D. Joseph and L. Preziosi, "Heat Waves," *Reviews of Modern Physics*, vol. 61, no. 1, pp. 41-73, 1989.
- [41] R. Kovacs and P. Rogolino, "Numerical treatment of nonlinear Fourier and Maxwell-Cattaneo-Vernotte heat transport equations," *International Journal of Heat and Mass Transfer*, vol. 150, 2019.
- [42] J. Liang, "Heat Transfer in Polymer Composites Filled with Inorganic Hollow Micro-Spheres," in *Heat Transfer in Multi-Phase Materials*, Heidelberg, Springer-Verlag Berlin Heidelberg, 2011, pp. 163-186.
- [43] COI Ceramics, Inc., "Properties of S200 CMC," [Online]. Available: <http://www.coiceramics.com/pdfs/2%20Non-oxide%20properties.pdf>. [Accessed 21 November 2020].
- [44] Engineers Edge, "Thermal Conductivity of Gases Chart," [Online]. Available: https://www.engineersedge.com/heat_transfer/thermal-conductivity-gases.htm. [Accessed 21 November 2020].
- [45] S. M. Shepard and M. F. Beemer, "Multilayer Material Characterizaion Using Thermographic Signal Reconstruction," in *AIP Conference Proceedings*, 2016.
- [46] D. Kopeliovich, "Advances in manufacture of ceramic matrix composites by infiltration techniques," in *Advances in Ceramic Matrix Composites Second Edition*, Duxford, Elsevier, 2018, pp. 93-119.
- [47] F. Christin, "CMC Materials for Space and Aeronautical Applications," in *Ceramic Matrix Composites*, Weinheim, Wiley-VCH Verlag GmbH & Co., 2008, pp. 327-352.

- [48] I. Low, "Advances in ceramic matrix composites: introduction," in *Advances in Ceramic Matrix Composites*, Duxford, Elsevier, 2018, pp. 1-7.
- [49] R. Naslain, "Foreward," in *Ceramic Matrix Composites*, Weinheim, Wiley-VCH Verlag GmbH & Co., 2008, pp. V-VIII.
- [50] COI Ceramics, Inc., "Silicon Carbide Ceramic Matrix Composites," [Online]. Available: www.coiceramics.com/nonoxidepg.html. [Accessed 1 February 2021].
- [51] SAE International, "CMH-17-5A Ceramic Matrix Composites Chapter 3: Processing, Characterization, and Manufacturing," in *Composites Material Handbook*, SAE, 2017, pp. 56-113.
- [52] U. Santhosh, J. Ahmad, G. Ojard, I. Smyth, Y. Gowayed and G. Jefferson, "Effect of porosity on the nonlinear and time-dependent behavior of Ceramic Matrix Composites," *Composites Part B*, vol. 184, 2019.
- [53] R. W. Gurney and N. F. Mott, "The Theory of the Photolysis of Silver Bromide and the Photographic Latent Image," *Proceedings of the Royal Society of London. Series A, Mathematical and Physical Sciences*, vol. 164, no. 917, pp. 151-167, 1938.
- [54] FUJIFILM Corporation, "Data Sheet Industrial Radiographic Systems," 2012. [Online]. Available: https://asset.fujifilm.com/www/us/files/2020-03/2c4dcf78dd4da9ea2216174a55527834/ix-film_datasheet.pdf. [Accessed 6 September 2021].
- [55] Iowa State University Center for Nondestructive Evaluation, "Discontinuities in TIG welds," [Online]. Available: <https://www.nde-ed.org/NDETechniques/Radiography/TechCalibrations/RadiographInterp.xhtml>. [Accessed 11 October 2021].
- [56] E. S. S. Nuez, "Attention to detail at its finest," United States Air Force, Lakenheath, 2014.
- [57] NDT Supply, "X-Rite 301 Transmission Densitometer," [Online]. Available: <https://ndtsupply.com/film-viewers-densitometers/densitometers/x-rite-301-transmission-densitometer/>. [Accessed 15 October 2021].
- [58] PerkinElmer Health Sciences, "Quantum FC microCT Imaging System User's Manual," March 2013. [Online]. Available: https://www.perkinelmer.com/Content/LST_Software_Downloads/9091.pdf. [Accessed 15 October 2021].

[59] Thermal Wave Imaging, Inc., "Products," [Online]. Available: <https://www.thermalwave.com/products/>. [Accessed 15 October 2021].

Appendix A: MATLAB Code

A.A.1: AreaAnalysis.m

```
function
[AreaData, EndTime, TimeData, TimeIndex, NormTime, NormTemp, LogTime, LogTemp, TempEq
, Temp1D, Temp2D, Threshold] =
AreaAnalysis(Data, length, FlashFrame, FrameRate) %Work on this.

    %prompt = 'What is the top left value? [x y] ';
    %[TLx, TLy] = input(prompt);
    prompt = 'What is the top left x-value value? ';
    TLx = input(prompt);
    prompt = 'What is the top left y-value value? ';
    TLy = input(prompt);
    %prompt = 'What is the bottom right value? [x y] ';
    %[BRx, BRy] = input(prompt);
    prompt = 'What is the bottom right x-value value? ';
    BRx = input(prompt);
    prompt = 'What is the bottom right y-value value? ';
    BRy = input(prompt);
    prompt = 'What is your 2nd Deriv PreTrim? [2] ';
    Trim1 = input(prompt);
    prompt = 'What is your 2nd Deriv End Trim? [240] ';
    Trim2 = input(prompt);

    AreaData = Data(TLy:BRy, TLx:BRx, :);

    EndTime = length * (1/FrameRate);

    TimeData = linspace(0, EndTime, length);

    TimeValue = TimeData(FlashFrame);

    PreFlashIndex = FlashFrame - 1;
    PreFlash = AreaData(:, :, 1:PreFlashIndex);
    PreFlashAvg = mean(PreFlash, 3);

    NormTime = TimeData - TimeValue;

    NormTemp = AreaData - PreFlashAvg;

    LogTime = log(NormTime(FlashFrame+1:end));

    LogTemp = log(abs(NormTemp(:, :, FlashFrame+1:end)));

    TempEq = zeros(size(LogTemp, 1), size(LogTemp, 2), size(LogTime, 2));
    Temp1D = zeros(size(LogTemp, 1), size(LogTemp, 2), size(LogTime, 2));
    Temp2D = zeros(size(LogTemp, 1), size(LogTemp, 2), size(LogTime, 2));

    for i = 1:size(LogTemp, 1)
        for j = 1:size(LogTemp, 2)
```

```

    plFit = polyfit(LogTime,transpose(squeeze(LogTemp(i,j,:))),5);
    TempEq(i,j,:) = polyval(plFit,LogTime);

    D1Fit = polyder(plFit);
    Temp1D(i,j,:) = polyval(D1Fit,LogTime);

    D2Fit = polyder(D1Fit);
    Temp2D(i,j,:) = polyval(D2Fit,LogTime);

    [Max(i,j),TimeIndex(i,j)] = max(squeeze(Temp2D(i,j,Trim1:end-
Trim2)));

    end
end

TimeTrim = NormTime(FlashFrame+Trim1:end-Trim2);

Threshold = TimeTrim(TimeIndex);

end

```

A.A.2: RawTiffConvert.m

```

[Data,width,height,length,FlashFrame,FrameRate] = OpenTWIRawFile();
length = size(Data,3);
%prompt = 'What is your file name? (include .tif)';
%filename = input(prompt);
[F,P] = uinputfile();
F = erase(F, ".mldatx");
F = [F, '.tif'];
fileName = fullfile(P,F);

for i=1:length
    SliceData=uint16(Data(:, :, i));
    %SliceData=(SliceData/16383)*65280;
    imwrite(SliceData,fileName, 'WriteMode', 'append');

end;

```

A.A.3: ThresholdImage.m

```

[Data,width,height,length,FlashFrame,FrameRate] = OpenTWIRawFile();
[AreaData,EndTime,TimeData,TimeIndex,NormTime,NormTemp,LogTime,LogTemp,TempEq
,Temp1D,Temp2D,Threshold] = AreaAnalysis(Data,length,FlashFrame,FrameRate);
ThresholdTif = uint16(Threshold*1000);
imwrite(ThresholdTif,'ThresholdTiff1.tif');

```



```
[F,P] = uinputfile();  
F = erase(F, ".mldatx");  
F = [F, '.tif'];  
fileName = fullfile(P,F);  
imwrite(ThresholdTif, fileName);
```